ARTseq-FISH reveals position-dependent fate decisions driven by cell cycle changes

Xinyu Hu[1,2], Bob van Sluijs[1,2], Óscar García Blay[1], Yury Stepanov[1], Koen Rietrae[1], Wilhelm T.S. Huck[1,*], Maike M. K. Hansen[1,*].

Affiliations:
[1]Institute for Molecules and Materials, Radboud University, Heyendaalseweg 135, 6525 AJ Nijmegen, the Netherlands.
[2]These authors contributed equally to this work: Xinyu Hu, Bob van Sluijs.
*Correspondence to: E-mail: w.huck@science.ru.nl (W.T.S.H); maike.hansen@ru.nl (M.M.K.H)

Abstract: Cell fate decisions are ubiquitous and play a critical role throughout development, yet how localization impacts cellular decision making remains unclear. To identify the drivers of position-dependent fate decisions at a molecular level, we developed a scalable antibody and mRNA targeting sequential fluorescence *in situ* hybridization (ARTseq-FISH) method capable of simultaneously profiling mRNAs, proteins and phosphoproteins in single cells at sub-micrometre spatial resolution. We studied 67 unique (phospho-)protein and mRNA targets in individual mouse embryonic stem cells (mESCs) cultured on circular micropatterns, yielding quantification of both abundance and localization of mRNAs and (phospho-)proteins during the first 48 hours of differentiation. ARTseq-FISH revealed a fate decision between continued self-renewal and differentiation that relies solely on the position of each mESC on the micropattern. Our results demonstrate that temporal changes in cell cycle orchestrate these position-dependent cell fate decisions.

Main

A complex interplay of signalling pathways and transcriptional networks guides morphological transformations during mammalian development[1-3]. During early development the balance between key signalling pathways defines the cellular choice between differentiation and self-renewal[4-6]. Intracellular networks provide pluripotent cells with the opportunity to make a decision: continue to self-renew by progressing through the cell cycle, or terminally differentiate by exiting the cell cycle during the G1 phase[6-8]. Micropatterning has successfully been used to mimic this decision and recapitulate early embryonic spatial patterning of germ layers[9-16]. However, it remains unknown how positioning on the micropattern impacts cellular decisions to ultimately define cell fate[9-16]. Specifically, the sequence of events that influence cell fate decisions on micropatterns and what factors drive the choice between self-renewal and differentiation remain unclear. To uncover how transcriptional, (post-)translational, and signalling pathways together orchestrate cell fate decisions, multiplexed quantitative spatial information at the single cell level is required. Therefore, to determine how mouse embryonic stem cells (mESCs) choose between continued self-renewal and differentiation, a scalable image-based spatial-multi-omics approach capable of simultaneously detecting and quantifying mRNAs and proteins with a high spatial resolution across large areas is required.

Recently, next generation sequencing (NGS)-based spatial-omics methods have greatly increased the multiplexing capacities of RNA or protein detection, albeit with low efficiency due to *in situ* reverse transcription and limited resolution of the beads used to capture targets[17-21]. Techniques that resolve the resolution issue, predominantly for RNA, are image-based spatial-omics methods. Image-based transcriptomic methods have greatly expanded the number of transcripts that can be resolved, using sequential fluorescence *in situ* hybridization (FISH)[22-27] and barcoding approaches. These methods have been combined with immunofluorescence (IF), but multiplexed protein detection remains a challenge[26]. For example, separate sequential experimental and imaging steps are often required to target and visualize RNAs and proteins, doubling experimental time[25]. Thus, scaling of these techniques in terms of multiplexing capabilities are bottlenecks, limiting the ability to simultaneously visualize mRNAs and proteins in high throughput[28-31]. Furthermore, the resolution of protein detection is below the level of the RNA detection proving a barrier to quantitative insights into protein location or spatial correlation of RNA and protein abundance[25-31].

Therefore, we developed a novel multiplexed spatial profiling method, antibody-mRNA targeted sequential FISH (ARTseq-FISH), that quantifies mRNA, protein and phosphoprotein abundances simultaneously in single cells[32]. By measuring the gene expression profile of 67 targets in individual cells during 48 hours of differentiation, we identify that the cellular decisions between continued self-renewal and differentiation is position-dependent. This position-dependent decision initiates after 24 hours of differentiation and becomes constant at 48 hours. Interestingly, this decision is caused by transient cell cycle changes that in turn differentially impact cell density depending on micropattern positioning. Ultimately, cell density drives position-based cell cycle changes that determine whether cells enter differentiation.

Results

ARTseq-FISH enables simultaneous visualization of mRNAs, proteins, and phosphoproteins

The ARTseq-FISH workflow comprises a series of consecutive steps (Fig. 1a and d, Extended Data Fig. 1-2, Supplementary Notes 1, Supplementary Fig. 1-14). In short, fixed cells are stained with DNA-barcoded antibodies against (phospho-)protein targets of choice

(Supplementary Table 1-2). The DNA-barcode of each antibodies contains a 10-nt polyadenylation (poly A) linker and a specific 36-nt sequence that is complementary to a corresponding target-specific single strand DNA (ssDNA) padlock probes (PLPs). On the other hand, cellular mRNAs are directly targeted by one specific ssDNA PLPs with a target sequence of 36-nt (Extended Data Fig.1 a-b), resulting in a DNA/RNA hybridization. Therefore, the circularizing of PLPs hybridized to proteins and RNAs require T4 DNA ligase and SplintR ligase respectively[33] (Fig.1a, Supplementary Fig. 2-4). Next, rolling circle amplification (RCA) generates large rolling circle products (RCPs) that amplify the original (phospho-)protein or mRNA target[33] (Fig. 1a and Supplementary Fig. 6). To decode the original target amplified by the RCPs, we first hybridize with target-specific bridge probes (BrPs), which are each recognized by unique combinations of fluorescently-labelled readout probes (RoPs) (Fig. 1a, Extended Data Fig.1c-d, Supplementary Fig. 7 and Supplementary Table 1), allowing the detection of diffraction limited spots for each mRNA and protein (Fig. 1b-c, Extended Data Fig.5). ARTseq-FISH provides similar relative protein abundance compared to classic immunofluorescence (Extended Data Fig.6a-d), and we determined a detection efficiency of ~90% (for Nanog mRNA) by comparing mRNA quantification using ARTseq-FISH with conventional single molecule RNA FISH (smFISH)[24] (Extended Data Fig.5e-h, Supplementary Table 3). In addition, ARTseq-FISH enhances the signal ~4-fold with respect to conventional smFISH (Extended Data Fig.5e-h), resulting in an average of less than 0.1 spots per cell detected as false positives (Supplementary Fig. 1).

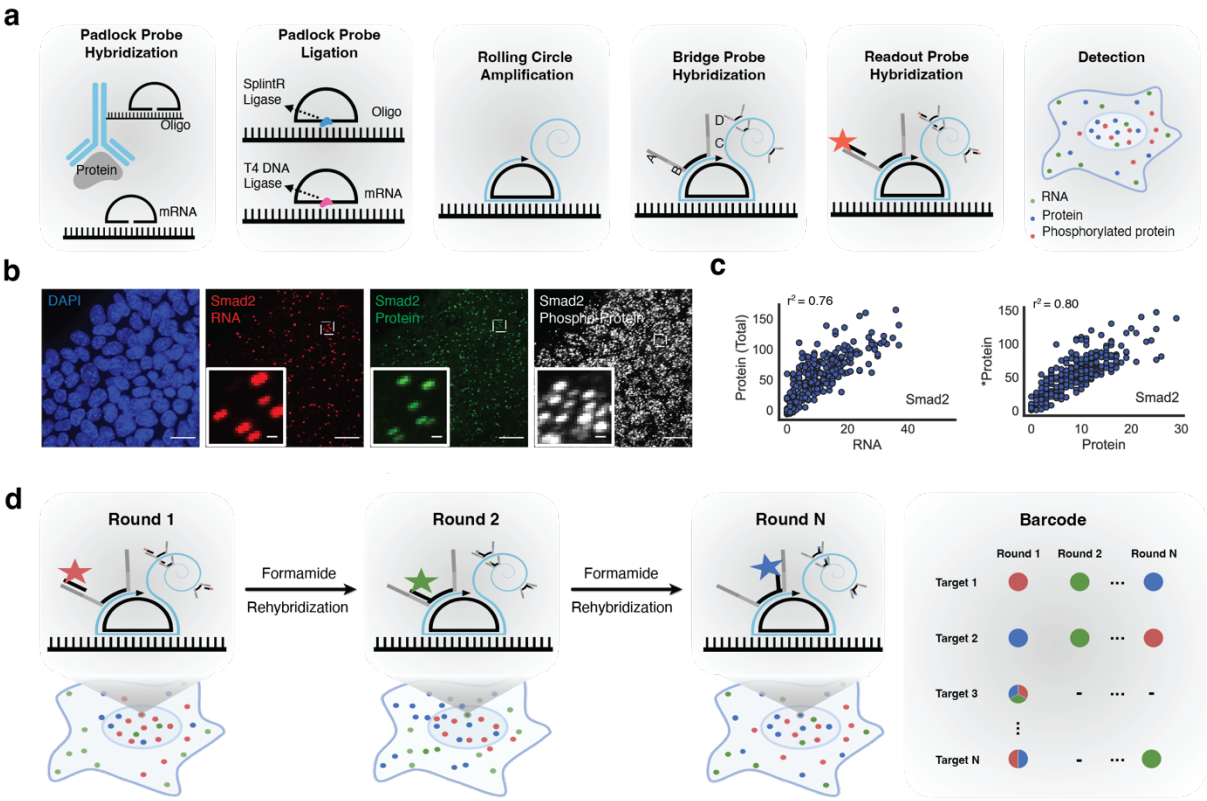

Fig. 1: Experimental outline of ARTseq-FISH. a, The experimental workflow of ARTseq-FISH that enables detection of different molecular species (mRNA, proteins, and phosphoproteins) simultaneously. Each antibody conjugated to oligonucleotides, targets its associated (phospho-)protein *in situ*. Target-specific PLPs bind to these oligonucleotides as well as cellular mRNA, respectively. Then the PLPs are circularized and amplified into RCPs. A set of target-specific BrPs hybridize to RCPs and then RoPs labelled with fluorophores bind to one of the four flanking sequences on the BrP. **b,** Raw data of simultaneously detecting Smad2 mRNA, protein and phosphoprotein with same resolution. Scale bar, 20 µm, 1 µm. **c,** Correlation between Smad2 mRNA and protein, Smad2 protein and phosphoprotein. **d,** The sequential stripping and rehybridization of a new known RoPs allows subsequent decoding of stacked signals.

Automated analysis and quantification of multiplexed mRNAs and proteins in single cells

Multiplexed, simultaneous detection and quantification of mRNAs and (phospho-)proteins over a large area is achieved by serial stripping and rehybridization of RoPs following a predetermined colour barcoding scheme (Fig. 1d, Methods, Supplementary Notes 1-2, Supplementary Fig. 12-14, Supplementary Table 4)[24]. The barcode of each target is determined by the presence of a given colour (green, red or far red) in a sequence of specific hybridization rounds. To decode the detected signal and translate this to mRNA or protein counts for individual cells, we developed an automated image analysis pipeline that returns the abundance of each target per cell.

The pipeline (Fig. 2a, more detailed description in Supplementary Notes 2, SN2 Fig. 1-3, software packages used[34-41]) initiates the analysis by identifying the local maxima per color channel[42] (ST2 Fig. 3-4) and classifying a signal as true using a support vector machine model (SVM) (ST2 Fig. 5-6). Single cell analysis requires reconstruction of single cells in 3D from the collection of images (Fig. 2a and SN2 Fig. 7-15). However, consistent segmentation is challenging because a segmentation algorithm that maps onto one nucleus might not map onto others (SN2 Fig. 8), or a global image filter that cleanly separates the nuclei in one image might not be optimal for another (SN2 Fig. 10). Therefore, an iterative approach was implemented, by repeatedly segmenting cells using different global image filters and segmentation parameters[43] (SN2 Fig. 9 and 13). We collected the segment labels and used an SVM model to filter out any failed segmentations. The remaining segmentation labels were subsequently used to reconstruct the cells in 3D by clustering their centroids with a node-based graph (SN2 Fig. 14-15). After interpolating any missing segments across the z-axis, we obtained a 3D bounding box. Another SVM model subsequently assessed if this bounding box contains a single cell. Before assigning mRNA and protein counts to segmented cells, we adjusted for any drift, by using the segmented cells as unique markers to align the images. Once a global shift was found, we refined the alignment by moving all hybridization signals across a narrow range of shifted pixels until the signals overlapped (SN2 Fig. 16-17). Ultimately, we decoded the overlapping signals and assigned each hybridization signal to a specific protein or mRNA in a specific cell (Fig. 2b, Extended Data Fig. 2 and 5, SN2 18-19).

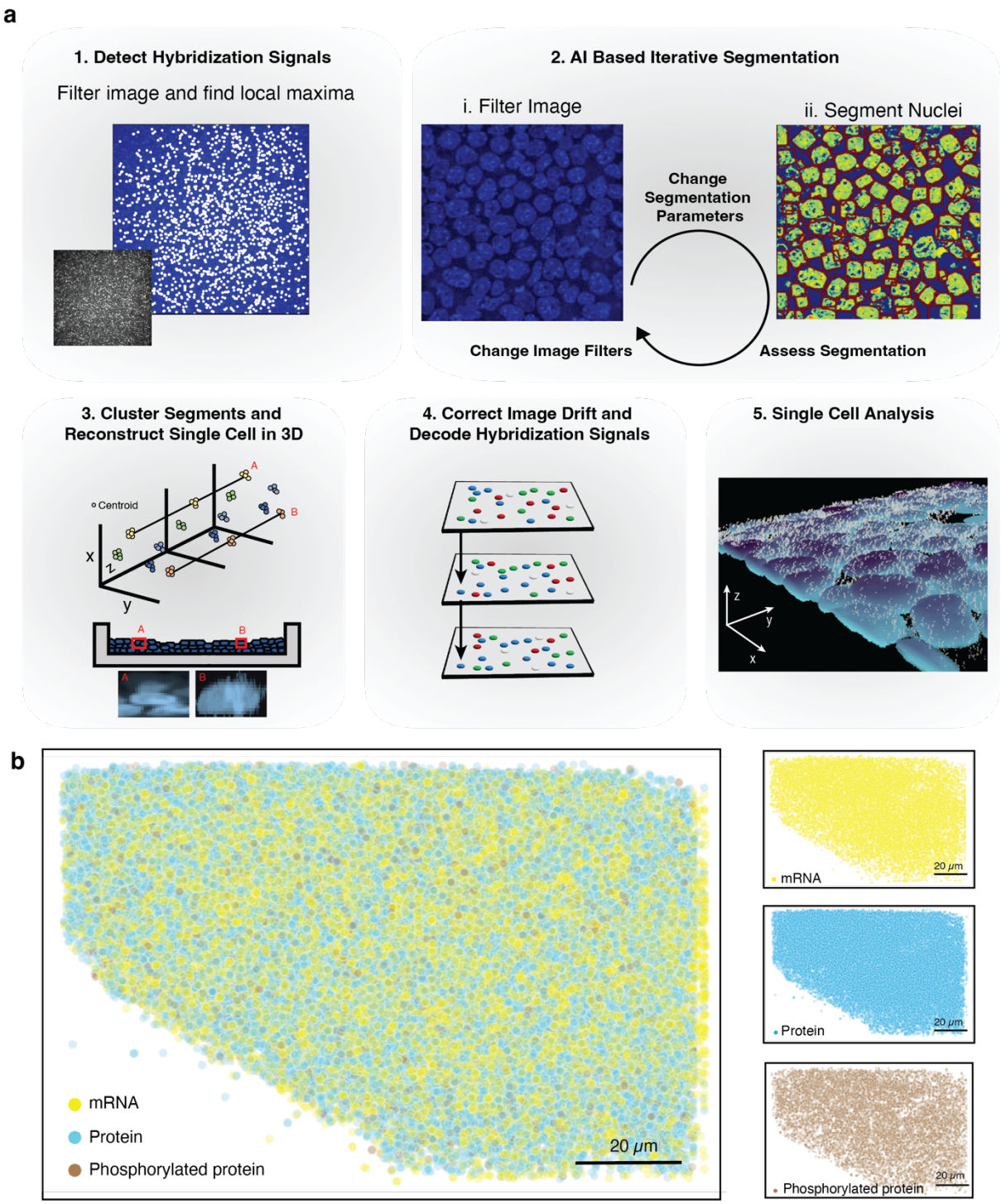

Fig. 2: Computational outline of ARTseq-FISH. a, A condensed summary of the automated computational pipeline that converts the raw microscope images into a single cell dataset, providing the abundance of each target per cell. First the hybridization signal is detected, followed by an iterative AI based segmentation approach, the segments are clustered, and the cells are reconstructed in 3D. Next, an image drift correction is applied to align the hybridization between rounds. In the final step these hybridization signals are decoded and assigned to the targets as well as individual cells. **b,** Reconstructed images show all the detected molecules in the cells cultured on micropattern 48 hours after leukemia inhibitory factor (LIF) withdrawal. The spots are subdivided into three classes: mRNA (yellow), protein (blue) and phosphorylated protein (brown). Scale bar, 20 µm.

149 **ARTseq-FISH profiles the expression of mRNAs, proteins and phosphoproteins in**
150 **individual mESCs**
151 To explore how the expression of mRNAs and (phospho-)proteins is affected during
152 differentiation on micropatterns and how this effects cell fate decisions, we exploited the
153 advantages of ARTseq-FISH. Leukemia inhibitory factor (LIF)/serum cultured mESCs are
154 heterogenous (Supplementary Fig. 15), because they are pluripotent cells that are capable of
155 making different cell fate decisions upon LIF withdrawal[44-46]. Therefore, we plated mESCs
156 directly on different sizes of the micropatterns (500 µm and 750 µm diameter) and withdrew
157 LIF from the serum medium for up to 48 hours to induce differentiation. After fixation, we
158 performed ARTseq-FISH on the micropatterned mESCs. Using our analysis pipeline, we
159 visualized the locations of unique mRNA and (phospho-)protein targets, (Fig. 3a) and
160 quantified the abundance of 67 targets in individual cells (Fig. 3a-d).
161
162 Among protein targets, lineage-associated markers i.e., N-cadherin, FOXA2, SNAIL, showed
163 higher abundance than pluripotency-related markers, i.e., Nanog, OCT4, STAT3, which is
164 expected in differentiating mESCs (Fig. 3b)[10, 11, 13]. ARTseq-FISH not only allows detection of
165 multiple mRNA and protein targets simultaneously but uniquely provides quantification of low
166 abundance targets—such as RB—due to the signal amplification step we incorporate (Extended
167 Data Fig.6a-d). Notably, while unphosphorylated RB shows low abundance at a protein level,
168 its mRNA and phospho-RB display higher expression levels than the average abundance (Fig.
169 3b-d). This is consistent with the cell cycle progression of LIF/serum cultured mESCs, where
170 the G1 phase is extremely short (~2 hours) due to the hyperphosphorylation of RB[47-49].
171 Furthermore, strong correlation of target counts between four different biological replicates
172 (Fig. 3e) demonstrate the high reproducibility of ARTseq-FISH (Extended Data Fig. 7 and SN2
173 Fig. 20).

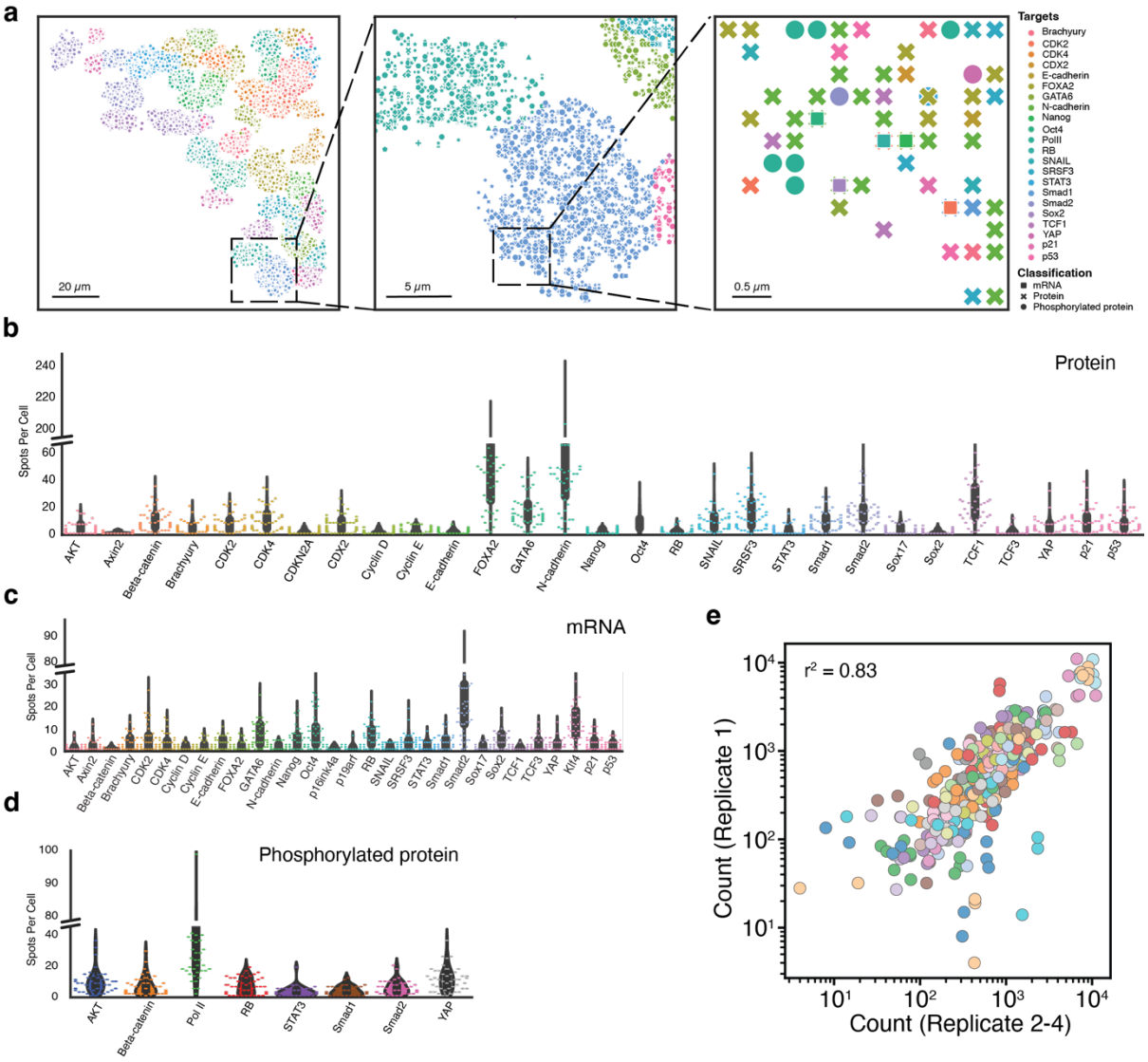

Fig. 3: ARTseq-FISH profiles the distribution of mRNAs and proteins in individual mESCs on micropatterns. a, Reconstructed images show the detected spots in (**a**) assigned to individual cells and the identity of these targets at a specific location. Scale bar, 20 μm, 5 μm, and 0.5 μm. **b-d,** Quantification of the single cell count abundance of proteins (**b**), mRNAs (**c**), and phosphorylated proteins (**d**). **e,** The scatter plot shows the average correlation between the total count of individual targets for 4 biological replicates at 48 hours differentiation of mESCs.

Single cell mRNA and (phospho-)protein expression profiles display gradients across micropattern differentiated mESCs

Unlike previous studies on micropattern-cultured ESCs[9-16], ARTseq-FISH provides single cell quantification (Fig. 1-3) of each molecular species while retaining precise spatial information. ARTseq-FISH data shows three distinct patterns of molecular distribution across mESCs on micropatterns: i) increased expression in cells located at the centre (i.e., p53); ii) evenly distributed throughout (i.e., phosphorylated RNA Pol II); and iii) highly expressed in cells at the periphery (i.e., Brachyury). These patterns were confirmed by immunofluorescence (Fig. 4a-c, Supplementary Fig. 16). Consistently, targets are classified into these three groups (Fig. 4d purple, white and orange respectively and Fig. 4e) and distributed distinctively according to their species, indicating reduced translation in the centre (Fig. 4d, pie chart). Furthermore, the correlation between mRNA and protein, total protein and phosphoprotein clusters into distinctive groups that appear position-dependent (Fig. 4f-g).

Lineage-associated markers: Brachyury, GATA6, and N-cadherin are enriched at the edge of the micropattern (Fig. 4d and Supplementary Fig. 17a). Furthermore, both phospho-Smad2 and Smad2 mRNA—i.e., the intracellular effector of NODAL pathway[50-52]—are more highly expressed at the edge of the micropattern (Fig. 4d and Supplementary Fig. 17b), where Smad2 is transcriptionally and post-translationally activated (Fig. 4f-g). Non-phosphorylated Smad2 is evenly distributed throughout the micropattern in line with its bifunctional roles in the regulation of both self-renewal and differentiation[50-52](Fig. 4d and f, Supplementary Fig. 17b**)**. Additionally, self-renewal-associated markers STAT3 and AKT, appear post-translationally inactivated at the edge of the micropattern (Fig. 4g). Together, multiplexed analysis of mRNA and (phospho-)protein indicate a decision to activate differentiation and downregulate self-renewal in cells located at the edge of the micropattern compared to the centre.

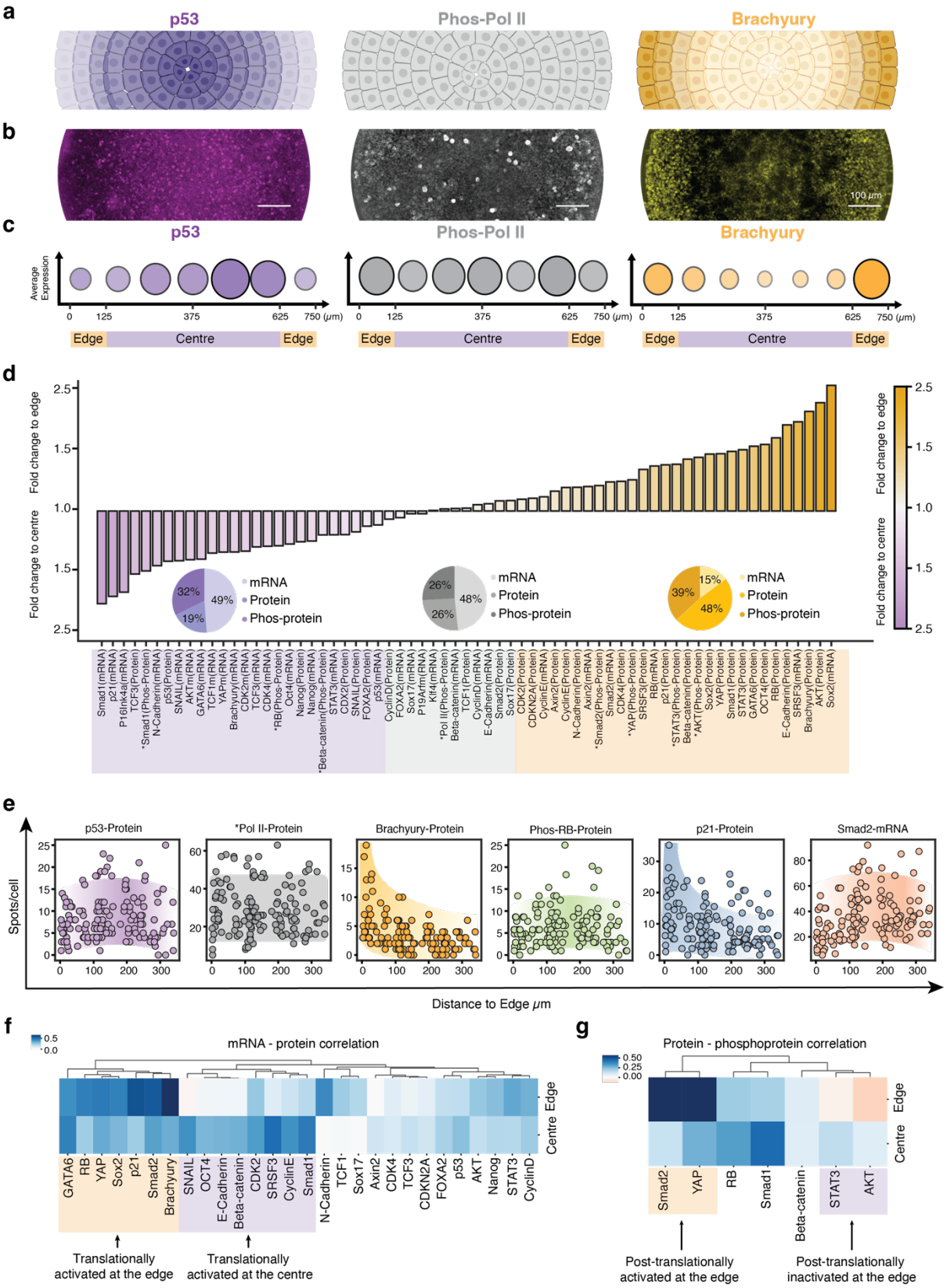

Fig. 4: ARTseq-FISH reveals gradients of mRNA and protein expression levels within micropattern-differentiated mESCs.

a, Schematic illustration of three representative spatial distributions of molecules on micropatterns. Created with BioRender.com. **b,** Immunofluorescence results of p53, Phosphorylated RNA Pol II, and Brachyury within a micropattern-differentiated mESCs. Scale bar, 100 µm. **c,** Average expression profile of spots per cell at seven positions across the micropattern for p53, Phosphorylated RNA Pol II, and Brachyury proteins (shaded area below x-axis illustrates the defined "edge" and "centre" of the micropattern). **d,** Mean fold changes of the expression

level of individual targets between edge and centre (purple and orange respectively). *: phosphorylated protein. Inset: pie chart showing the percentage of mRNAs, proteins and phosphoproteins in each area. **e,** The spots per cell (y-axis) with respect to the position of the cell on the micropattern (x-axis) of selected targets. The edge of the micropattern serves as the reference value for the relative position of the cells. Cells are found at the edge at 0 µm and near the centre at 375 µm. **f,** Cluster map of the single cell correlation between mRNAs and respective proteins depending on the position on the micropattern (edge and centre). Gene clusters that are translationally activated at the edge or the centre show a higher correlation between their mRNA and protein at the edge or centre respectively. **g,** Cluster map of the correlation between proteins and their respective phosphorylated protein with respect to the position on the micropattern (edge and centre).

Temporal ARTseq-FISH reveals position-dependent cell fate decisions

To determine the drivers of position-dependent fate decisions, we studied the spatial distribution of molecules across micropatterned cells at different time points (0 hours, 24 hours, and 48 hours) after LIF withdrawing (Fig. 5a). As differentiation progresses, the expression profiles within individual cells are successively segregated from each time point (Fig. 5b and SN2 Fig. 21-22). Furthermore, at 0 hours cells at the edge or the centre are not segregated from one another, however, at 24 hours after LIF withdrawal the position-favoured expression profiles on the micropattern start appearing and become more striking after 48 hours (Fig. 5c). This is in line with observed changes in Brachyury protein over time (Fig. 5d and Supplementary Fig. 18e). Together, this data suggests a position-based difference in molecular expression profiles that appears during differentiation on the micropattern and was not present in pre-differentiated cells (Fig. 5d and Supplementary Fig. 18).

Since cells with higher RB protein expression experience a longer G1 phase, whereas cells with higher phospho-RB enter a rapid cell cycle with a short G1 phase[46-48], the observed RB gradient indicates position-based differences in cell cycle over time (Fig. 4d-g and Fig. 5d-f). Importantly, at 48 hours of differentiation, p21 protein is more abundant in cells found at the edge where less phospho-RB is expressed (Fig. 4e, Supplementary Fig. 17c-d, Fig. 5d and Supplementary Fig. 18c-d). Upregulation of p21 leads to an inhibition of the CDK/Cyclin complex in turn regulating the phosphorylation of RB protein (Fig. 5f), which would result in a prolonged G1 phase[46-48, 53]. Conversely, p21 protein, as well as RB mRNA and protein are more abundant in the cells at the edge, where cells presented increased lineage associated proteins (Fig. 5d-f). Notably, on our 750 µm diameter micropatterns (Extended Data Fig. 8), cell density shows two radially symmetric peaks over time, approximately 100 µm from the edge of the micropattern (Fig. 5g), indicating that the colonies are not flat but somewhat 'donut' shaped. Both targets enriched at the edge (i.e., Brachyury and p21 protein) and at the centre (i.e., Smad1 mRNA and phospho-RB) show negative correlation with cell density (Extended Data Fig. 8f), indicating that position rather than cell density defines the cell decision. Unsurprisingly, p53 is more abundant at the bottom of the micropattern where more abnormal nuclei were observed and cells might become apoptotic (Fig. 5h-i, Extended Data Fig. 8a-b, d-e). p53 abundance is also positively correlated to cell density (Extended Data Fig. 8f). These results reveal that the observed gradient of differentiation is not correlated to cell density on the micropattern, but appears associated with changes in expression of cell cycle related genes, which in turn show position-dependent differences[54].

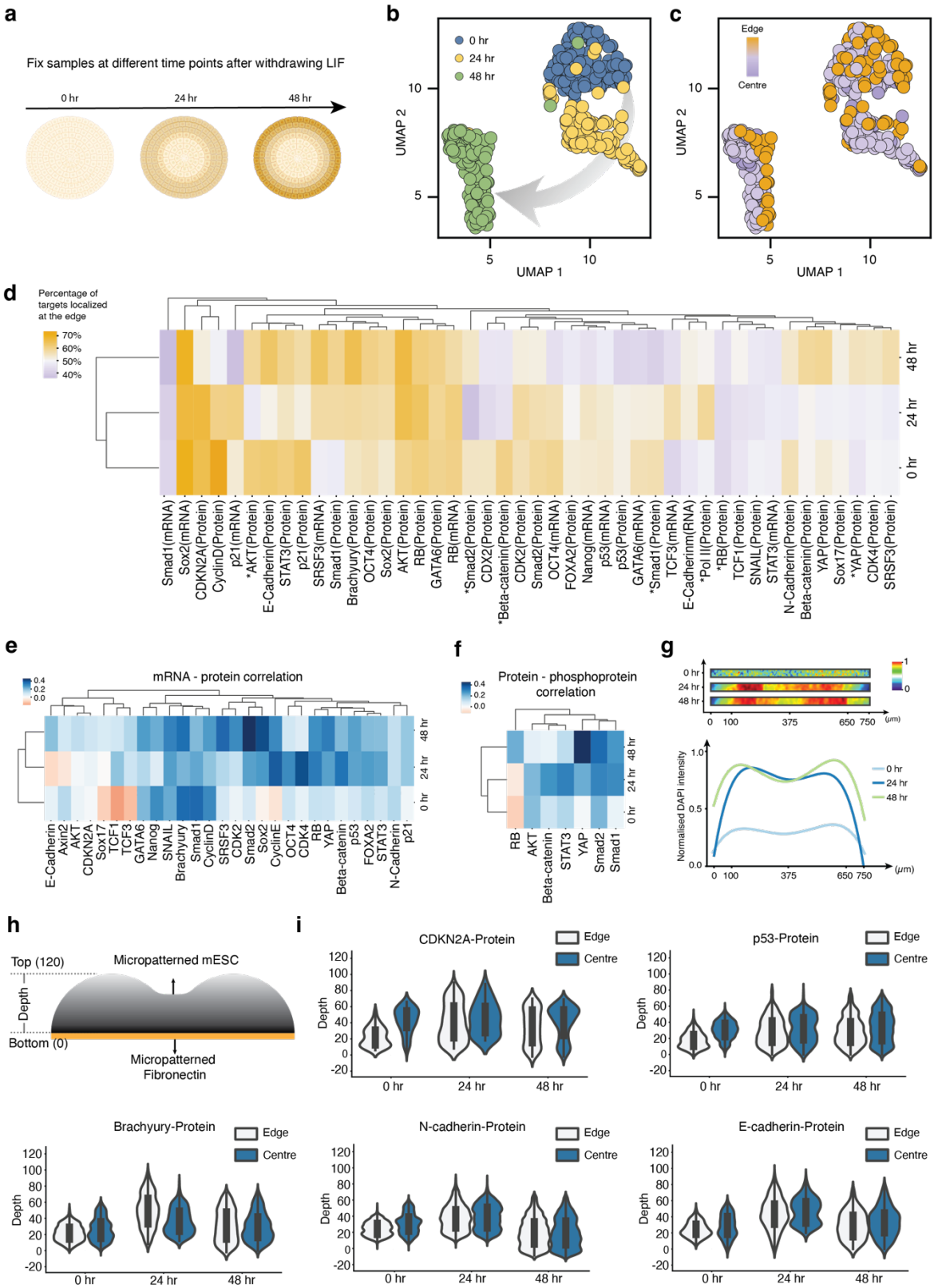

Fig. 5: Spatial-temporal quantification of mRNAs and proteins during mESCs differentiation on micropatterns. a, Schematic of the experiment, sampling at 0, 24 and 48 hours during the differentiation process. Created with BioRender.com. **b,** UMAP clustering of the individual cells within the three experiments of different time points during differentiation. **c,** the same UMAP, but cells are shaded for the position (edge or centre) within the micropattern (orange and purple respectively). **d,** The single cell expression gradient of individual targets across the micropattern. *: phosphorylated protein. **e,** Correlation between mRNA and total protein of selected targets over time. **f,** Correlation between non phosphorylated protein and phosphorylated protein of selected targets over time. **g,** Normalized DAPI intensity across the micropattern (750 µm diameter) over time. **h,**

Schematic of the depth of the micropatterned mESCs. **i,** the depth distribution of selected targets at the edge and centre of the micropattern over time. The width of the violin plot represents the relative abundance.

Cell fate decisions between self-renewal and differentiation are driven by cell cycle changes

Finally, we sought to decipher the sequence of events that governs the observed position-dependent fate decision between continued self-renewal and differentiation. To this end, we divided targets into three groups according to their respective functions: cell cycle, differentiation and self-renewal (Supplementary Table 5). Both self-renewal and cell cycle associated molecules show distinguishable divergence over time at both the edge and centre of micropatterns (Fig. 6a-c, Supplementary figure 19). Interestingly, both changes in self-renewal and cell cycle genes precede changes in differentiation related molecules (Fig. 6a-c, blue, orange and green respectively).

To identify position-based gene expression patterns over time, we performed pseudo time analysis (SN2 Fig. 23-25)[55]. Surprisingly, most molecules involved in cell cycle, differentiation, and self-renewal showed similar expression trajectories in cells located at the centre of micropattern (Fig. 6d-f and Extended Data Fig. 9). Yet, after 48 pseudo time hours, the location on the micropattern (i.e., centre) enforces a choice to senescence[56](Extended Data Fig. 8d-f) which is accompanied by a reduction in both self-renewal and differentiation potential[4](Fig. 6e-f, Brachyury and AKT, STAT3). Continued proliferation is impeded due to the limited space available on the micropattern (Fig. 5g, maximum density reached after 24 hours), explaining the stark drop in expression of cell cycle, differentiation and self-renewal related targets after 40 pseudo time hours (Fig. 6d-f, centre).

DAPI intensity differences[57-59] indicate temporal changes in the cell cycle at both the edge and centre (Fig. 6g-h, Supplementary figure 20a and SN2 Fig. 7), which in turn indicate differences in proliferation rate at the edge versus the centre (Fig. 6h, Extended Data Fig. 8c and Supplementary figure 20b). At the edge, increased proliferation generates a distinct gradient of cell density (Fig. 5g and Extended Data Fig. 8c), which causes an upregulation of lineage marker expression (Fig. 6e, Extended Data Fig. 8f and Supplementary figure 19)[9, 10, 12]. After 48 hours cells at the edge enter and remain in the G1 phase (Fig. 6h), from which they enter the terminal differentiation stage[7, 49]. In contrast, cells at the centre upregulate proteins involved in cell cycle, differentiation and self-renewal (Fig. 6d-f, 0-24 hours), yet, due to less proliferation (Fig. 6h, 0-24 hours) these cells fail to terminally differentiate (Fig. 6d-f, Extended Data Fig. 10 and Supplementary figure 19). These expression profiles depend on the shape of the micropattern, which impacts cell cycle distribution, cell density gradient, and ultimately cell fate decisions (Extended Data Fig. 10). Due to the limited space on the centre of the micropattern (i.e., limited accessibility to nutrients, Fig. 5g), proliferation is downregulated (Fig. 6h, 24-48 hours, Fig 5g, 24-48 hours) and cells with more p53 (Fig. 4a-c, 4g, Fig. 5d and 5h-i) and CDKN2A (Fig. 5h-i) undergo apoptosis and senescence independently of the cell density profile (Fig. 5g, Extended Data Fig. 8)[56, 60-62]. Although apoptosis and senescence play essential roles in early stage of mammalian development[63-65], apoptosis and senescence observed here are likely due to space-based limitations on the micropattern[9-16].

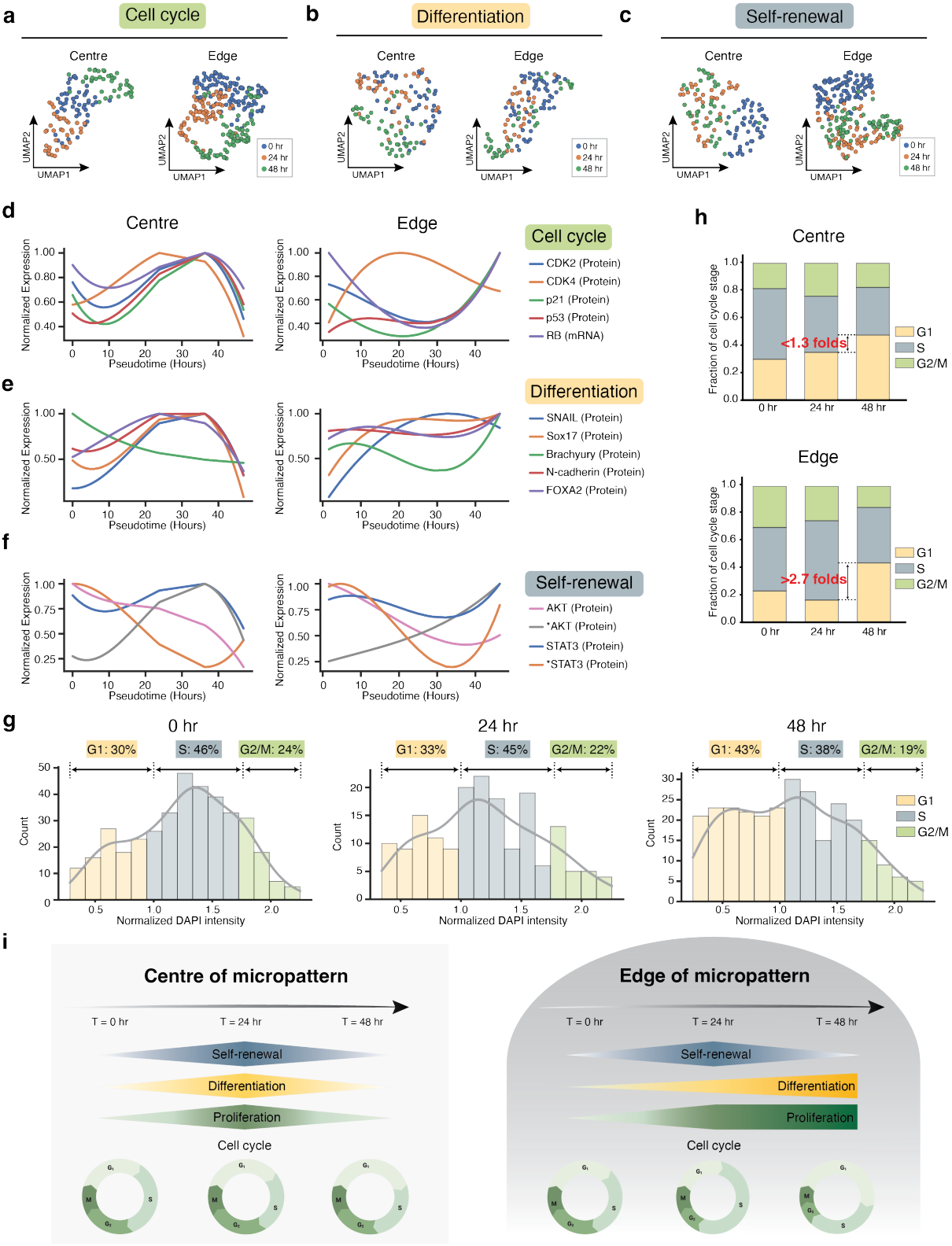

Fig. 6: The position-dependent fate decision of mESCs on micropattern differentiation is linked to changes in cell cycle phase.

a-c, UMAP shows the expression levels of cell cycle **(a)**, differentiation **(b)**, and self-renewal **(c)** related targets at the centre and edge of the micropattern at 0 hours, 24 hours and 48 hours of differentiation. **d-f,** Pseudo time analysis of the expression trajectories of cell cycle **(d)**, differentiation **(e)**, and self-renewal **(f)**, associated molecules at the centre and edge of the micropattern during the differentiation process. **g,** Histogram of cell cycle

phases of cells at 0 hours, 24 hours and 48 hours of differentiation. **h,** Fraction of cell cycle stages in cells located at the centre and the edge of the micropattern. **i,** Schematics illustrates the theory that mESCs located at different positions (i.e., the centre and the edge) of the micropattern experience different cell cycle paces when they make fate decisions. Partially (cell cycle phases) created with BioRender.com.

Discussion

Thus far, there have been two major areas of focus when studying micropatterned cells: i) implementation of immunohistochemistry (IHC) to determine spatial-temporal protein abundance in low throughput[9-16]; or ii) revealing the emergence of specific cell types by single-cell transcriptomic sequencing in high throughput, with limited spatial information[11]. It is therefore necessary to exploit a technique that provides quantitative spatial information on different functional proteins and their respective mRNAs at same time during differentiation. More importantly, the dynamic expression and low abundance of cell cycle related markers makes cell cycle regulation difficult to study *in situ*. This is critical to explore how cell cycle, self-renewal, and differentiation related molecules behave during differentiation.

ARTseq-FISH, a novel multiplexed spatial profiling method described here, enables simultaneous measurement and quantification of mRNAs and (phospho-)proteins in individual cells. The combined protocol of mRNA and protein detection not only provides the same resolution of different molecular species but is also highly scalable (Fig. 1). Additionally, the deep learning-based image analysis pipeline in ARTseq-FISH (Fig. 2) precisely identifies the cells and FISH signals, which allowed detection of 67 mRNAs, proteins, and phosphoproteins simultaneously (Fig. 3). We applied ARTseq-FISH to micropattern differentiation and identified the position-dependent fate decision of differentiating mESCs. The analysis revealed the expression level of individual cells and their dependence on the respective location on the micropattern (Fig. 4) during differentiation of mESCs (Fig. 5). Intriguingly, cells located at the edge and centre of the micropattern obtain completely different molecular expression profiles over time (Fig. 6). ARTseq-FISH demonstrates that cell cycle control underlies the position-dependent decision to either continue self-renewing or differentiating. Taken together, our findings provide a theory about position-dependent linage commitment on micropattern differentiation: cells found at different positions within a micropattern generate different expression profiles during the differentiation stimulation, which determines the fate decisions of cells when they exit the G1 phase.

352 **Methods**
353 **Cell culture**
354 mESC-E14 (mESCs) in this study were obtained from Hendrik Marks's group at Radboud
355 University [66]. The culture plates were coated with 0.1% gelatin (Sigma Aldrich, 48723-500G).
356 Undifferentiated mESCs were cultured and maintained in the medium consisting of high
357 glucose-Dulbecco's Modified Eagles Medium (Gibco™, 41965039) supplemented with 15%
358 fetal bovine serum (Gibco™, A3840002), 2 mM L-glutamine (Gibco™, A2916801), 1 mM
359 sodium pyruvate (Gibco™, 11360039), 1% penicillin–streptomycin (Gibco™, 15140122), 0.1
360 mM beta-mercaptoethanol (Gibco™ 31350010) and 500 U/mL recombinant leukemia
361 inhibitory factor (LIF; Millipore, ESG1107) at 37 °C in 5% CO_2. Cells were passaged every 2-
362 3 days using 0.05% Trypsin/EDTA (Gibco™, 25300062). Cell density was 5x 10^4 per well for
363 the experiments in the μ-Slide (ibidi, 81501) and 1x $10^4/cm^2$ for the experiments in the μ-Slide
364 3D perfusion (ibidi, 80376). For differentiation assays, cells were cultured on micropatterns in
365 LIF medium for 1 day and then changed to a medium without LIF (-LIF) for up to 2 days.
366
367 **Micropatterned Substrate Fabrication**
368 Micropatterned islands with different diameters (750 μm and 500 μm) were produced on a
369 silicon mask using standard photolithography [67]. Distances between the microfeatures were
370 100 μm and the height of the microfeatures was between 50 μm and 100 μm. The PDMS and
371 the curing agent (SYLGARD 184, 1.1KG) was mixed with a ratio of 10:1 in a plastic beaker.
372 The PDMS mixture was degassed to remove the air bubbles under vacuum. Then, the degassed
373 PDMS mixture was poured onto the master in a petri dish. A gel was formed in a 60°C oven
374 over night. Finally, the gel PDMS stamps was peeled off the master.
375 The μ-Slide 3D perfusion microchambers were plasma oxidized to improve protein printing
376 efficiency and cell attachment on the glass bottoms [68]. The surface of the PDMS stamps was
377 placed with a drop of 50 μg/mL fibronectin in PBS and incubated for 1 hour at room
378 temperature. The PDMS stamps were washed twice with PBS and dried thoroughly. The glass
379 bottoms of μ-Slide 3D perfusion were then coated with the fibronectin from the PDMS stamps,
380 followed by the graft of the PLL (20)-g [3.5]- PEG (2) (0.1 mg/mL, SuSoS AG) in 10 mM
381 HEPES (Gibco™, 15630080) for 30 minutes at room temperature. The PLL-g-PEG prevents
382 cell attachment in the nonprinted areas [69].
383 **Immunostaining**
384 Cells were fixed with 4% paraformaldehyde (PFA) (Sigma Aldrich, 1040021000-1L) for 10
385 minutes at room temperature and then permeabilized with 0.5% Triton in 1x PBS at room
386 temperature for 10 minutes. Cells were washed with 1x PBS three times after fixation and
387 permeabilization. After permeabilization, cells were incubated in blocking buffer (5% BSA in
388 1x PBS containing 0.5% Triton) for 1 hour at room temperature. The primary antibodies were
389 diluted in blocking buffer and incubated at room temperature for 2-4 hours. Cells were then
390 washed with 1x PBS three times and then incubated in secondary antibody solution for 2 hours
391 at room temperature. The secondary antibodies were diluted 1:1000 in 1x PBS. DAPI (10
392 μg/mL) (Thermo Scientific™ 62247) staining was performed together with secondary
393 antibodies.
394
395 **smFISH**
396 Probes of Nanog were purchased from Stellaris (LGC Biosearch Technologies, Novato, CA)
397 (http://www.singlemoleculefish.com/). Each set contains 28 probes and each probe is 20 nt
398 long (Table S1). Probes are conjugated with TAMRA. Cells were fixed with 4% PFA (Sigma
399 Aldrich, 1040021000-1L) for 10 minutes at room temperature and then permeabilized with pre-
400 chilled 70% EtOH at 4°C for a minimum of 1 hour. Cells were washed three times with 1x
401 PBS. Probes were diluted to a final concentration of 50 nM in 1 g/mL dextran sulfate (Sigma,

402 catalog # 42867), 2x SSC and 10% formamide (Invitrogen, AM9342). The hybridization of the
403 probes was performed overnight at 37°C. The next day, samples were washed with 2x SSC
404 buffer at 37°C for 30 minutes and then incubated with DAPI solution (diluted in 2x SSC) at
405 37°C for 15-20 minutes. Cells were washed with 2x SSC and then switch to a photo-protective
406 buffer containing 50% glycerol (Thermo Fisher Scientific, Waltham, MA), 75 µg/mL glucose
407 oxidase (Sigma Aldrich, Darmstadt, Germany), 520 µg/mL catalase (Sigma Aldrich,
408 Darmstadt, Germany), and 0.5 mg/mL Trolox (Sigma Aldrich, Darmstadt, Germany). Samples
409 were imaged with a spinning disk confocal microscope (OLYMPUS PlanXApo 60x/1.42- N.A.
410 oil-immersion objective, and Andor iXon camera). DAPI was excited by 405 nm, and TAMRA
411 was excited by 540 nm lasers. The distance of Z-stacks was set to 0.5 µm. The exposure time
412 and laser intensity were set to reach a maximum gray value of 16000 each image.
413
414 **Probe design of ARTseq-FISH**
415 The mRNA sequences were obtained from NCBI website (Mus musculus). Probes were
416 designed according to the targeted regions by using online software
417 (http://biosearchtech.com/stellaris-designer/), for individual probe sequences see Table S1. For
418 targeting RNA directly, we selected 36 nt from the mRNA sequence (18 nt for 5' arm and 18
419 nt for 3'arm of PLP). Each PLP contains two arms (18 nt each) for binding to the targeting
420 region, one unique 28 nt sequence identical to the bridge probe and one common RCA primer
421 binding region. Besides the 28 nt sequences identical to paired PLPs, BrPs consist of four
422 overhang sequences with 18 nt each.
423
424 Oligonucleotides used for antibody conjugation consist of a 10 nt linker (polyA) and a 36 nt
425 sequences corresponding to the complementary PLP. The 36 nt sequences for antibody
426 conjugation, 28 nt sequences of PLPs and BrPs, and 18nt readout probe sequences were
427 identified using a previously published algorithm [70]. The readout probes are 18 nt in length and
428 labeled with three different fluorophores (ATTO488, TAMRA, CY5). We used BLAST from
429 NCBI to check that the 18 nt probe sequence is less than 13 nt (<70%) complementary to other
430 Mus musculus transcripts. All the probes have GC content within the range 45%-65% and were
431 purchased from Integrated DNA technologies (IDT).
432

Oligonucleotides (46 nt)	**5'- Azide-AAAAAAAAAA- [36 nt unique sequence] -3'**
Padlock probe (84 nt)	5' -phosphorylated- [18 nt 5'-arm] - [28 nt unique sequence] - [20 nt RCA primer] - [18 nt 3'- arm] - 3'
Bridge probe (108 nt)	5' - [readout 1] -AA- [readout 2] -AA- [28 nt unique sequence] -AA- [readout 3] -AA- [readout 4] - 3'

433
434 **Antibody–DNA conjugation**
435 Antibodies (Abs) used in ARTseq-FISH were labelled with DNA oligonucleotides as previous
436 described [71]. In brief, Abs were first buffer exchanged into 0.2 M NaHCO3 (pH 8.3) (Thermo
437 Scientific Acros 217125000) by using Zeba™ Spin Desalting Columns, 40K MWCO (Thermo
438 Scientific™ 87767). Abs were then reacted with 10x molar excess of dibenzocyclooctyne-S-
439 S-N-hydroxysuccinimidyl (DBCO-S-S-NH) ester (Sigma Aldrich, 761532-1mg) for 2 hours at
440 room temperature in the dark. Next, Abs were purified using Zeba™ Spin Desalting Columns,
441 40K MWCO to remove excess DBCO-s-s-NHS. 5' Azide modified DNA oligonucleotides
442 (IDT) were incubated with Abs (molar ratio of antibody to single-stranded DNA of 1:15)
443 overnight at 4°C in the dark. The conjugated Abs were buffer exchanged into PBS (Gibco™
444 20012019) containing 0.05% sodium azide (Sigma Aldrich, S8032-25G) and 0.1 mM EDTA
445 (Lonza, 51201), and excess oligos were removed by 100K Amicon centrifuge filters (Merck
446 UFC510096). The DNA-conjugated Abs were stored at 4°C. The list of antibodies and

447 corresponding DNA oligonucleotides is provided in Table S1 and S2. The dilution of
448 conjugated antibodies was optimized between ratios of 1:1000, 1:2000 and at 1:4000 and the
449 ratio of 1:4000 was used for ARTseq-FISH.
450
451 **ARTseq-FISH**
452 ***Fixation and permeabilization*** Cells were fixed with 4% PFA (Sigma Aldrich, 1040021000-
453 1L) for 10 minutes at room temperature and then permeabilized with pre-chilled 100%
454 methanol at -20°C for 10 minutes. Cells were washed with 1x PBS three times after fixation
455 and permeabilization.
456 ***Blocking and Primary antibody incubation*** After permeabilization, cells were incubated in
457 blocking buffer (5% BSA in PBS containing 0.5% Triton) for 1 hour at room temperature. The
458 DNA oligonucleotide labelled primary antibodies were diluted to 1:4000 in blocking buffer
459 and incubated at room temperature for 2-4 hours.
460 ***RNA PLP hybridization and ligation*** Phosphorylated PLPs were hybridized to the mRNA
461 sequences directly at a final concentration of 100 nM/PLP. The reaction was performed
462 overnight at 37°C using 1x Ampligase ligase buffer (Lucigen, A1905B), 50 mM KCl
463 (Invitrogen, AM9640G), 20% Formamide (Invitrogen, AM9342), 0.2 µg/µL tRNA, 1U/ µL
464 RiboLock RNase Inhibitor (Thermo Scientific, EO0381) and 0.2 µg/µL of BSA in Nuclease-
465 free water (Invitrogen, AM9937). Next, PLP ligation was performed for 4 hours at room
466 temperature using 0.5 U/µl SplintR Ligase (NEB, M0375), 1x Ampligase ligase buffer, 10 µM
467 ATP (Invitrogen, 18330019) and 0.2 µg/µL of BSA in Nuclease-free water.
468 ***Ab PLP hybridization and ligation*** The hybridization of PLPs to DNA oligonucleotides
469 conjugated to Abs was performed at a final concentration of 5 nM/PLP. The ligation of PLPs
470 was performed in the same reaction with T4 DNA ligase, 1x T4 DNA ligase buffer, 50 mM
471 KCl (Invitrogen, AM9640G), 20% Formamide (Invitrogen, AM9342), 0.2 µg/µL of BSA and
472 Nuclease-free water. This reaction was incubated at 37°C for 30 minutes followed by 45°C for
473 90 minutes.
474 ***Rolling circle amplification (RCA)*** RCA was performed with 0.5 U/µL Phi29 polymerase
475 (NEB, M0269L), 1x Phi29 polymerase buffer, 5% Glycerol (Sigma, G5516), 0.25 mM each
476 dNTP (Thermo Scientific, R0192), 0.2 U/µL Exonuclease I (Thermo Scientific, EN0581), 0.2
477 µM RCA primer and 0.2 µg/µL of BSA in Nuclease-free water overnight at 30˚C.
478 ***Bridge probe hybridization*** BrPs were hybridized at a final concentration of 100 nM per probe.
479 The reaction took place in the hybridization buffer which contains 2x SSC, 20% formamide,
480 0.05 g/mL dextran sulfate and nuclease-free water, for 1-2 hours at room temperature. An extra
481 fixation with 4% PFA was performed to stabilize the binding of bridge probes and rolling circle
482 amplification products.
483 ***Readout probe hybridization*** RoPs were hybridized at a final concentration of 100 nM per
484 probe and in the same hybridization buffer as the BrPs. The reaction can be performed together
485 with DAPI (10 µg/mL) (Thermo Scientific™ 62247) staining for 1h at room temperature. Cells
486 were washed with 2x SSC and then switch to a photo-protective buffer containing 50% glycerol
487 (Thermo Fisher Scientific, Waltham, MA), 75 µg/mL glucose oxidase (Sigma Aldrich,
488 Darmstadt, Germany), 520 µg/mL catalase (Sigma Aldrich, Darmstadt, Germany), and 0.5
489 mg/mL Trolox (Sigma Aldrich, Darmstadt, Germany).
490 ***Image acquisition*** Images of sequential hybridization were acquired with a spinning disk
491 confocal microscope (OLYMPUS PlanXApo 60x/1.42- N.A. oil-immersion objective, and
492 Andor iXon camera). DAPI was excited by 405 nm, and ATTO488, TAMRA, Cy5 was excited
493 by 475 nm, 540 nm and 638 nm lasers respectively. The distance of Z-stacks was set as 0.5 µm.
494 The exposure time and laser intensity were set differently in different channels to obtain the
495 same maximum intensity value of spots.
496

Flow cytometry analysis of cell cycle

mESCs were seeded in 1.9 cm^2 wells (24-well format) with a density of 4.4x 10^3 cells/cm^2. The wells were previously coated with 0.1% gelatin. Cells were seeded in serum/LIF medium and cultured for 24 hours. Then, cells were fixed in pre-chilled 70% ethanol for 30 minutes at -20°C and washed by 1x PBS. Finally, cells were stained with 1 µg/mL propidium iodide (Sigma-Aldrich, P4864-10ML) containing 10 µg/mL RNaseA (VWR International B.V, 0675-250MG) for 15 minutes. After staining, cells were transferred to a flow cytometry tube and kept on ice until their immediate analysis in a BD FACS Calibur™ flow cytometer.

Flow cytometry analysis of Nanog-GFP mESC cell line in serum/LIF conditions

The Nanog-GFP mESC line was kindly provided by Leor Weinberger's lab (Gladstone Institutes) [72]. Nanog-GFP mESCs and non-labeled mESCs were seeded in 9.5 cm^2 wells (6-well format) with a density of 4x 10^4 cells/cm^2. The wells were previously coated with 0.1% gelatin. Cells were seeded in serum/LIF medium. 24 hours post-seeding, cells were detached with 400 µL of 0.05% trypsin-EDTA for 2 minutes and resuspended in growing media. Cells were transferred to a flow cytometry tube and kept on ice until their immediate analysis in a BD FACS Calibur™ flow cytometer.

Flow cytometry analysis of CD24 expression in mESC

mESCs were seeded in 1.9 cm^2 wells (24-well format) with a density of 4.4x 10^3 cells/cm^2. The wells were previously coated with 0.1% gelatin. Cells were seeded in serum/LIF medium and cultured for 96 hours, with a medium renewal at 48 hours of culture. Cells were stained with an anti-mouse CD24 antibody conjugated to alexa647 fluorophore (BioLegend, 101818) or an alexa647 isotype control antibody (BioLegend, 400626) for 30 minutes in serum/LIF media at 37˚C. After staining, cells were washed with 1x PBS and detached with accutase (StemCell™ technologies, 07922) for 5 minutes at 37˚C, transferred to a flow cytometry tube and kept on ice until their analysis in a BD FACSVerse™ flow cytometer.

Image and data analysis

Details described in Supplementary Information, Supplementary Note 2: Computational pipelines development of ARTseq-FISH.

Data availability

All data is available in the main text or the supplementary information.

References

1. Rivron, N.C. et al. Blastocyst-like structures generated solely from stem cells. *Nature* **557**, 106-111 (2018).
2. Martyn, I., Kanno, T.Y., Ruzo, A., Siggia, E.D. & Brivanlou, A.H. Self-organization of a human organizer by combined Wnt and Nodal signalling. *Nature* **558**, 132-135 (2018).
3. Girgin, M.U. et al. Bioengineered embryoids mimic post-implantation development in vitro. *Nat Commun* **12**, 5140 (2021).
4. Lolas, M., Valenzuela, P.D.T., Tjian, R. & Liu, Z. Charting Brachyury-mediated developmental pathways during early mouse embryogenesis. *Proceedings of the National Academy of Sciences* **111**, 4478-4483 (2014).
5. Li, Z. et al. BMP4 Signaling Acts via Dual-Specificity Phosphatase 9 to Control ERK Activity in Mouse Embryonic Stem Cells. *Cell Stem Cell* **10**, 171-182 (2012).
6. Pauklin, S. & Vallier, L. The Cell-Cycle State of Stem Cells Determines Cell Fate Propensity. *Cell* **155**, 135-147 (2013).
7. Zhao, M.L. et al. Molecular Competition in G1 Controls When Cells Simultaneously Commit to Terminally Differentiate and Exit the Cell Cycle. *Cell Reports* **31**, 107769 (2020).
8. Lengthened G1 Phase Indicates Differentiation Status in Human Embryonic Stem Cells. *Stem Cells and Development* **22**, 279-295 (2013).
9. Blin, G. et al. Geometrical confinement controls the asymmetric patterning of brachyury in cultures of pluripotent cells. *Development* **145**, dev166025 (2018).
10. Martyn, I., Brivanlou, A.H. & Siggia, E.D. A wave of WNT signaling balanced by secreted inhibitors controls primitive streak formation in micropattern colonies of human embryonic stem cells. *Development* **146** (2019).
11. Minn, K.T. et al. High-resolution transcriptional and morphogenetic profiling of cells from micropatterned human ESC gastruloid cultures. *Elife* **9** (2020).
12. Etoc, F. et al. A Balance between Secreted Inhibitors and Edge Sensing Controls Gastruloid Self-Organization. *Developmental Cell* **39**, 302-315 (2016).
13. Morgani, S.M., Metzger, J.J., Nichols, J., Siggia, E.D. & Hadjantonakis, A.K. Micropattern differentiation of mouse pluripotent stem cells recapitulates embryo regionalized cell fate patterning. *Elife* **7** (2018).
14. Chhabra, S., Liu, L., Goh, R., Kong, X. & Warmflash, A. Dissecting the dynamics of signaling events in the BMP, WNT, and NODAL cascade during self-organized fate patterning in human gastruloids. *PLoS Biol* **17**, e3000498 (2019).
15. Tewary, M. et al. A stepwise model of reaction-diffusion and positional information governs self-organized human peri-gastrulation-like patterning. *Development* **144**, 4298-4312 (2017).
16. Jaiswal, S.K., Raj, S. & DePamphilis, M.L. Developmental Acquisition of p53 Functions. *Genes (Basel)* **12** (2021).
17. Merritt, C.R. et al. Multiplex digital spatial profiling of proteins and RNA in fixed tissue. *Nat Biotechnol* **38**, 586-599 (2020).
18. Vickovic, S. et al. High-definition spatial transcriptomics for in situ tissue profiling. *Nat Methods* **16**, 987-990 (2019).
19. Liu, Y. et al. High-Spatial-Resolution Multi-Omics Sequencing via Deterministic Barcoding in Tissue. *Cell* **183**, 1665-1681 e1618 (2020).
20. Stahl, P.L. et al. Visualization and analysis of gene expression in tissue sections by spatial transcriptomics. *Science* **353**, 78-82 (2016).
21. Chen, A. et al. Spatiotemporal transcriptomic atlas of mouse organogenesis using DNA nanoball-patterned arrays. *Cell* **185**, 1777-1792.e1721 (2022).

22. Foreman, R. & Wollman, R. Mammalian gene expression variability is explained by underlying cell state. *Molecular Systems Biology* **16**, e9146 (2020).
23. Shaffer, S.M., Wu, M.-T., Levesque, M.J. & Raj, A. Turbo FISH: A Method for Rapid Single Molecule RNA FISH. *PLOS ONE* **8**, e75120 (2013).
24. Eng, C.H.L. et al. Transcriptome-scale super-resolved imaging in tissues by RNA seqFISH. *Nature* **568**, 235-+ (2019).
25. Takei, Y. et al. Integrated spatial genomics reveals global architecture of single nuclei. *Nature* **590**, 344-350 (2021).
26. Wang, G., Moffitt, J.R. & Zhuang, X. Multiplexed imaging of high-density libraries of RNAs with MERFISH and expansion microscopy. *Sci Rep-Uk* **8**, 4847 (2018).
27. Moffitt, J.R. et al. High-performance multiplexed fluorescence in situ hybridization in culture and tissue with matrix imprinting and clearing. *P Natl Acad Sci USA* **113**, 14456-14461 (2016).
28. Rao, A., Barkley, D., Franca, G.S. & Yanai, I. Exploring tissue architecture using spatial transcriptomics. *Nature* **596**, 211-220 (2021).
29. Wang, F. et al. RNAscope: a novel in situ RNA analysis platform for formalin-fixed, paraffin-embedded tissues. *J Mol Diagn* **14**, 22-29 (2012).
30. Popovic, D., Koch, B., Kueblbeck, M., Ellenberg, J. & Pelkmans, L. Multivariate Control of Transcript to Protein Variability in Single Mammalian Cells. *Cell Syst* **7**, 398-411 e396 (2018).
31. Schulz, D. et al. Simultaneous Multiplexed Imaging of mRNA and Proteins with Subcellular Resolution in Breast Cancer Tissue Samples by Mass Cytometry. *Cell Syst* **6**, 25-36 e25 (2018).
32. Taniguchi, Y. et al. Quantifying E. coli Proteome and Transcriptome with Single-Molecule Sensitivity in Single Cells. *Science* **329**, 533-538 (2010).
33. Lee, H., Salas, S.M., Gyllborg, D. & Nilsson, M. Direct RNA targeted transcriptomic profiling in tissue using Hybridization-based RNA In Situ Sequencing (HybRISS). *bioRxiv*, 2020.2012.2002.408781 (2020).
34. Collaboration, T.A. et al. Astropy: A community Python package for astronomy. *A&A* **558**, A33 (2013).
35. Zhou, Q.-Y., Park, J. & Koltun, V. Open3D: A modern library for 3D data processing. *arXiv preprint arXiv:1801.09847* (2018).
36. Bradski, G. The openCV library. *Dr. Dobb's Journal: Software Tools for the Professional Programmer* **25**, 120-123 (2000).
37. Waskom, M.L. Seaborn: statistical data visualization. *Journal of Open Source Software* **6**, 3021 (2021).
38. McKinney, W. in Proceedings of the 9th Python in Science Conference, Vol. 445 51-56 (Austin, TX, 2010).
39. Sainburg, T., McInnes, L. & Gentner, T.Q. Parametric UMAP: learning embeddings with deep neural networks for representation and semi-supervised learning. (2020).
40. McInnes, L., Healy, J. & Melville, J. Umap: Uniform manifold approximation and projection for dimension reduction. *arXiv preprint arXiv:1802.03426* (2018).
41. Pedregosa, F. et al. Scikit-learn: Machine learning in Python. *the Journal of machine Learning research* **12**, 2825-2830 (2011).
42. Hansen, M.M.K., Desai, R.V., Simpson, M.L. & Weinberger, L.S. Cytoplasmic Amplification of Transcriptional Noise Generates Substantial Cell-to-Cell Variability. *Cell Systems* **7**, 384-397.e386 (2018).
43. van Sluijs, B., Maas, R.J.M., van der Linden, A.J., de Greef, T.F.A. & Huck, W.T.S. A microfluidic optimal experimental design platform for forward design of cell-free genetic networks. *Nature Communications* **13**, 3626 (2022).

44. Acampora, D. et al. Functional Antagonism between OTX2 and NANOG Specifies a Spectrum of Heterogeneous Identities in Embryonic Stem Cells. *Stem Cell Reports* **9**, 1642-1659 (2017).
45. Guo, G. et al. Serum-Based Culture Conditions Provoke Gene Expression Variability in Mouse Embryonic Stem Cells as Revealed by Single-Cell Analysis. *Cell Rep* **14**, 956-965 (2016).
46. Marks, H. et al. The Transcriptional and Epigenomic Foundations of Ground State Pluripotency. *Cell* **149**, 590-604 (2012).
47. Ter Huurne, M., Chappell, J., Dalton, S. & Stunnenberg, H.G. Distinct Cell-Cycle Control in Two Different States of Mouse Pluripotency. *Cell Stem Cell* **21**, 449-455 e444 (2017).
48. ter Huurne, M. et al. Critical Role for P53 in Regulating the Cell Cycle of Ground State Embryonic Stem Cells. *Stem Cell Reports* **14**, 175-183 (2020).
49. DeVeale, B. et al. G1/S restriction point coordinates phasic gene expression and cell differentiation. *Nature Communications* **13**, 3696 (2022).
50. Sakaki-Yumoto, M., Liu, J., Ramalho-Santos, M., Yoshida, N. & Derynck, R. Smad2 Is Essential for Maintenance of the Human and Mouse Primed Pluripotent Stem Cell State*. *Journal of Biological Chemistry* **288**, 18546-18560 (2013).
51. Senft, A.D. et al. Combinatorial Smad2/3 Activities Downstream of Nodal Signaling Maintain Embryonic/Extra-Embryonic Cell Identities during Lineage Priming. *Cell Reports* **24**, 1977-1985.e1977 (2018).
52. Liu, L. et al. Nodal is a short-range morphogen with activity that spreads through a relay mechanism in human gastruloids. *Nature Communications* **13**, 497 (2022).
53. Pack, L.R., Daigh, L.H., Chung, M. & Meyer, T. Clinical CDK4/6 inhibitors induce selective and immediate dissociation of p21 from cyclin D-CDK4 to inhibit CDK2. *Nat Commun* **12**, 3356 (2021).
54. O'Duibhir, E. et al. Cell cycle population effects in perturbation studies. *Molecular Systems Biology* **10**, 732 (2014).
55. Street, K. et al. Slingshot: cell lineage and pseudotime inference for single-cell transcriptomics. *BMC Genomics* **19**, 477 (2018).
56. Liu, J.-Y. et al. Cells exhibiting strong p16^{INK4a} promoter activation in vivo display features of senescence. *Proceedings of the National Academy of Sciences* **116**, 2603-2611 (2019).
57. Ferro, A. et al. Blue intensity matters for cell cycle profiling in fluorescence DAPI-stained images. *Laboratory Investigation* **97**, 615-625 (2017).
58. Olofsson, K., Carannante, V., Takai, M., Önfelt, B. & Wiklund, M. Single cell organization and cell cycle characterization of DNA stained multicellular tumor spheroids. *Sci Rep-Uk* **11**, 17076 (2021).
59. Roukos, V., Pegoraro, G., Voss, T.C. & Misteli, T. Cell cycle staging of individual cells by fluorescence microscopy. *Nat Protoc* **10**, 334-348 (2015).
60. Najjary, S. et al. Combination therapy with miR-34a and doxorubicin synergistically induced apoptosis in T-cell acute lymphoblastic leukemia cell line. *Medical Oncology* **38**, 142 (2021).
61. de la Rosa, E.J. & de Pablo, F. Cell death in early neural development: beyond the neurotrophic theory. *Trends in Neurosciences* **23**, 454-458 (2000).
62. He, H. et al. p53 and p73 Regulate Apoptosis but Not Cell-Cycle Progression in Mouse Embryonic Stem Cells upon DNA Damage and Differentiation. *Stem Cell Reports* **7**, 1087-1098 (2016).

63. Agnello, M., Bosco, L., Chiarelli, R., Martino, C. & Roccheri, M.C. The Role of Autophagy and Apoptosis During Embryo Development. *Cell Death - Autophagy, Apoptosis and Necrosis*, 83-112 (2015).
64. Storer, M. et al. Senescence is a developmental mechanism that contributes to embryonic growth and patterning. *Cell* **155**, 1119-1130 (2013).
65. Muñoz-Espín, D. et al. Programmed cell senescence during mammalian embryonic development. *Cell* **155**, 1104-1118 (2013).
66. van Mierlo, G. et al. Integrative Proteomic Profiling Reveals PRC2-Dependent Epigenetic Crosstalk Maintains Ground-State Pluripotency. *Cell Stem Cell* **24**, 123-137.e128 (2019).
67. Théry, M. & Piel, M. Adhesive micropatterns for cells: a microcontact printing protocol. *Cold Spring Harb Protoc* **2009**, pdb.prot5255 (2009).
68. van Kooten, T.G., Spijker, H.T. & Busscher, H.J. Plasma-treated polystyrene surfaces: model surfaces for studying cell-biomaterial interactions. *Biomaterials* **25**, 1735-1747 (2004).
69. Bao, M., Xie, J., Piruska, A. & Huck, W.T.S. 3D microniches reveal the importance of cell size and shape. *Nat Commun* **8**, 1962 (2017).
70. Moffitt, J.R. et al. High-throughput single-cell gene-expression profiling with multiplexed error-robust fluorescence in situ hybridization. *Proc Natl Acad Sci U S A* **113**, 11046-11051 (2016).
71. Rivello, F. et al. Single-cell intracellular epitope and transcript detection reveals signal transduction dynamics. *Cell Reports Methods* **1**, 100070 (2021).
72. Desai, R.V. et al. A DNA repair pathway can regulate transcriptional noise to promote cell fate transitions. *Science* **373**, eabc6506 (2021).

Acknowledgments

We thank members of the Huck and Hansen laboratories for the thoughtful discussion and suggestions; Aigars Piruska for making the silicon masters with micropatterns and technical assistance with CSU spinning disk confocal; Erik van Buijtenen and Kinga Matuła for sharing the antibody conjugation protocols, and fruitful discussions and suggestions from Erik van Buijtenen. We also thank Hendrik Marks for his generous gift of mESC-E14 cell line and thoughtful suggestions. We acknowledge generous support from Radboud University (W.T.S.H.), the Christine Mohrmann fellowship (M.M.K.H), and the Netherlands Organization for Scientific Research (NWO) (ENW-XS awards OCENW.XS3.055 and OCENW.XS21.2.050, both M.M.K.H., and a Spinoza grant, W.T.S.H.). X.H. acknowledges financial support from the China Scholarship Council (CSC).

Author information

Authors and Affiliations

Institute for Molecules and Materials, Radboud University, Heyendaalseweg 135, 6525 AJ Nijmegen, the Netherlands

Xinyu Hu, Bob van Sluijs, Óscar García Blay, Yury Stepanov, Koen Rietrae, Wilhelm T.S. Huck, Maike M. K. Hansen.

Contributions

X.H., B.v.S., W.T.S.H., and M.M.K.H. conceived and designed the study. X.H. developed and optimized the experimental procedure for ARTseq-FISH. B.v.S. developed the software for ARTseq-FISH. Ó.G.B. helped with probe design and optimization of ARTseq-FISH workflow. Ó.G.B., also conducted supporting experiments. Y.S., and K.R., contributed to validation experiments of ARTseq-FISH. X.H., B.v.S., W.T.S.H., and M.M.K.H. wrote the manuscript and Ó.G.B. edited the manuscript.

Corresponding author

Correspondence to Wilhelm T.S. Huck and Maike M. K. Hansen.

Ethics declarations

Competing interests

Authors declare no competing interests.

733 **Extended data**

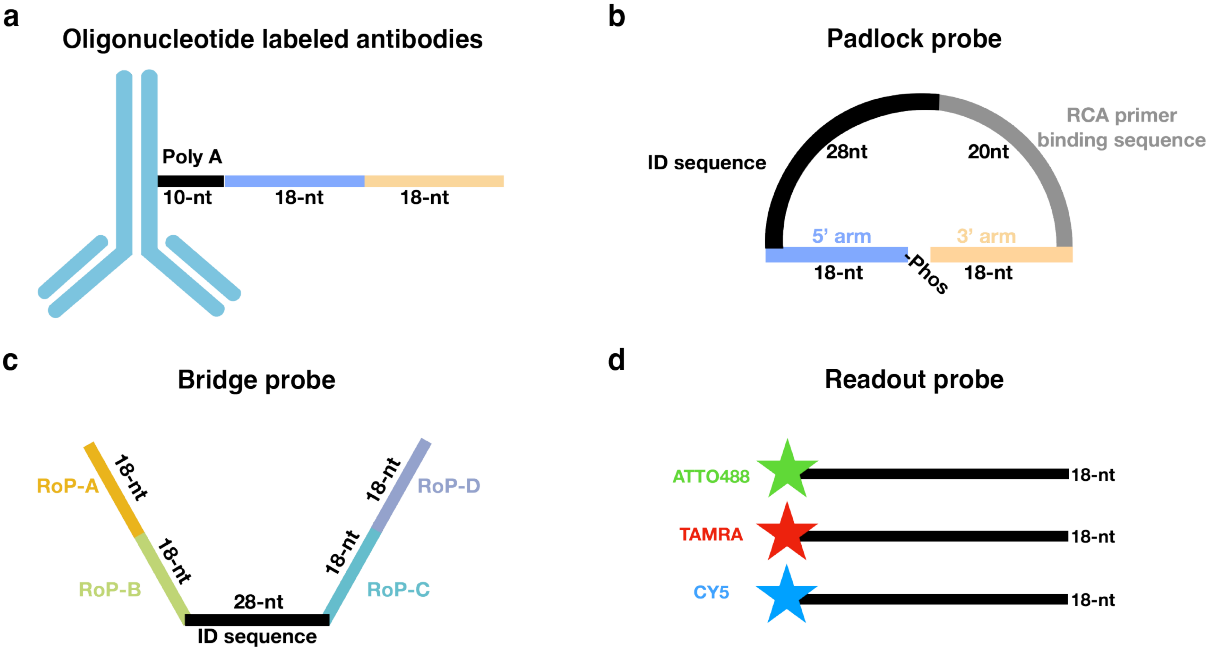

734

735 **Extended Data Fig. 1: Schematics of oligonucleotides labeled antibody and probes in**
736 **ARTseq-FISH.**
737 **a,** The oligonucleotide labeled to antibodies are designed as 10 nt polyadenylate and two 18 nt
738 sequences (purple and light-yellow lines) complementary to unique padlock probes. **b,** PLPs
739 consist of two 18 nt sequences (purple and light-yellow lines) recognizing the oligonucleotides
740 of protein targets or cellular mRNAs, a 28 nt ID sequence (black line) for corresponding to
741 unique bridge probes, and a 20 nt RCA primer binding sequence. **c,** BrPs are composed of a 28
742 nt ID sequence (black line) identical to the ID sequence of padlock probes, four 18nt sequences
743 for different readout probes binding. **d,** RoPs are an 18 nt single strand DNA conjugated with
744 three different fluorophores (ATTO488, TAMRA and CY5).

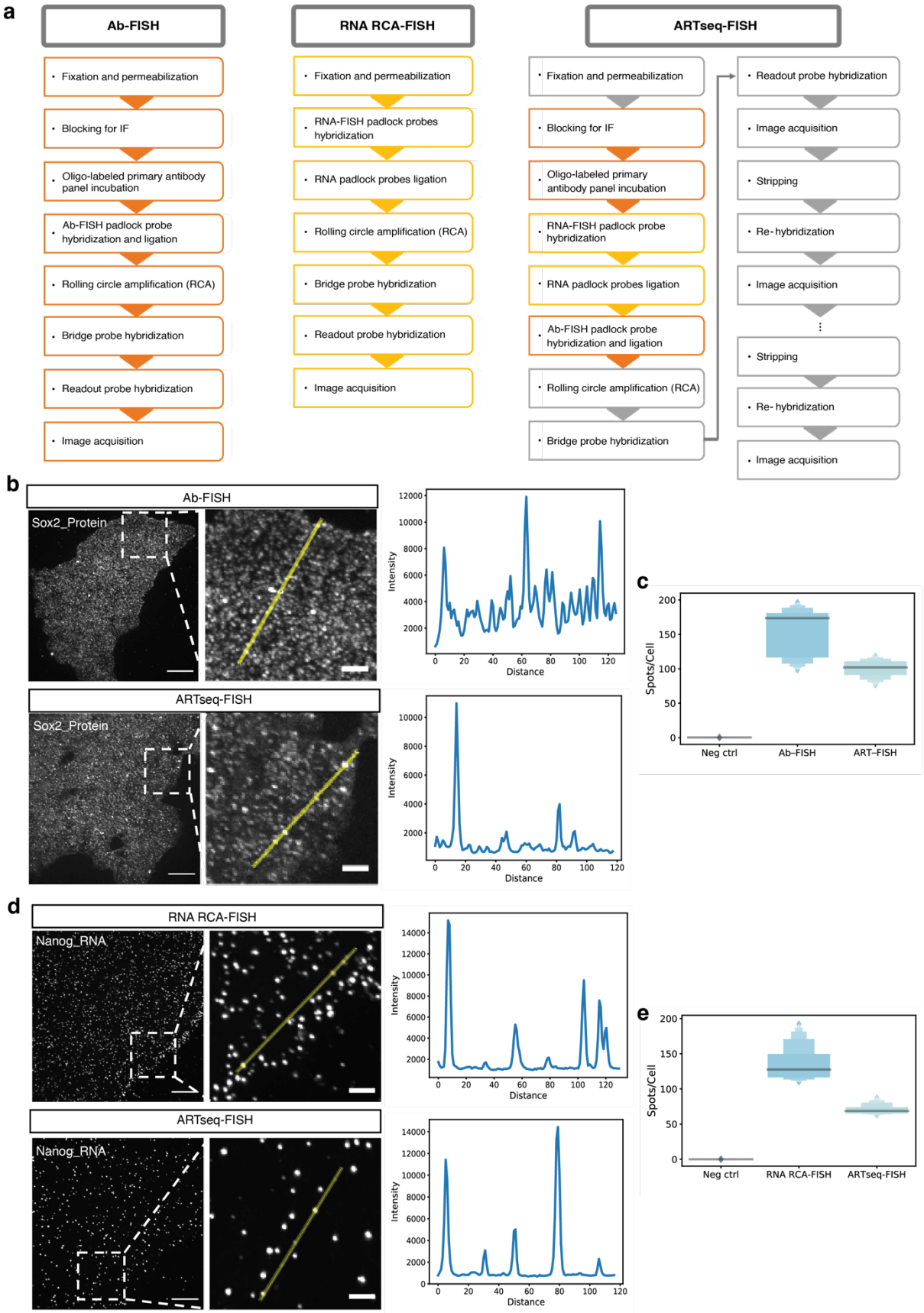

Extended Data Fig. 2: Generation of the ARTseq-FISH.
a, Flow chart of the experimental procedures showing protein and mRNA detection separately and simultaneously with ARTseq-FISH. The protocols of Ab-FISH and RNA RCA-FISH are

749 demonstrated in orange and yellow boxes respectively. The simultaneous protein and mRNA
750 detection protocol, i.e., ARTseq-FISH, is illustrated by orange, yellow and gray boxes, which
751 show the Ab-FISH specific-, RNA RCA-FISH specific, and combined steps respectively. **b,**
752 Representative max intensity and Z projection images of Sox2 protein detection by Ab-FISH
753 and ART-FISH. Line plots showed the intensity of the selected spots in zoomed images. Scale
754 bar, 20 µm, 5 µm. **c,** Quantification of spots per cell of Sox2 protein detected by Ab-FISH and
755 ARTseq-FISH. Neg ctrls were performed by ARTseq-FISH protocols without PLPs added.
756 (Neg ctrl n=362, Ab-FISH n=256, ARTseq-FISH n=291). **d,** Representative max intensity Z
757 projection images of Nanog mRNA detection by RNA RCA-FISH and ART-FISH. Line plots
758 show the intensity of the selected spots in zoomed images. Scale bar, 20 µm, 5 µm. **e,**
759 Quantification of spots per cell of Nanog mRNA detected by RNA-FISH and ARTseq-FISH.
760 Neg ctrl were performed by ARTseq-FISH protocols without PLPs added. (Neg ctrl n=360,
761 RNA RCA-FISH n=1193, ARTseq-FISH n=454).

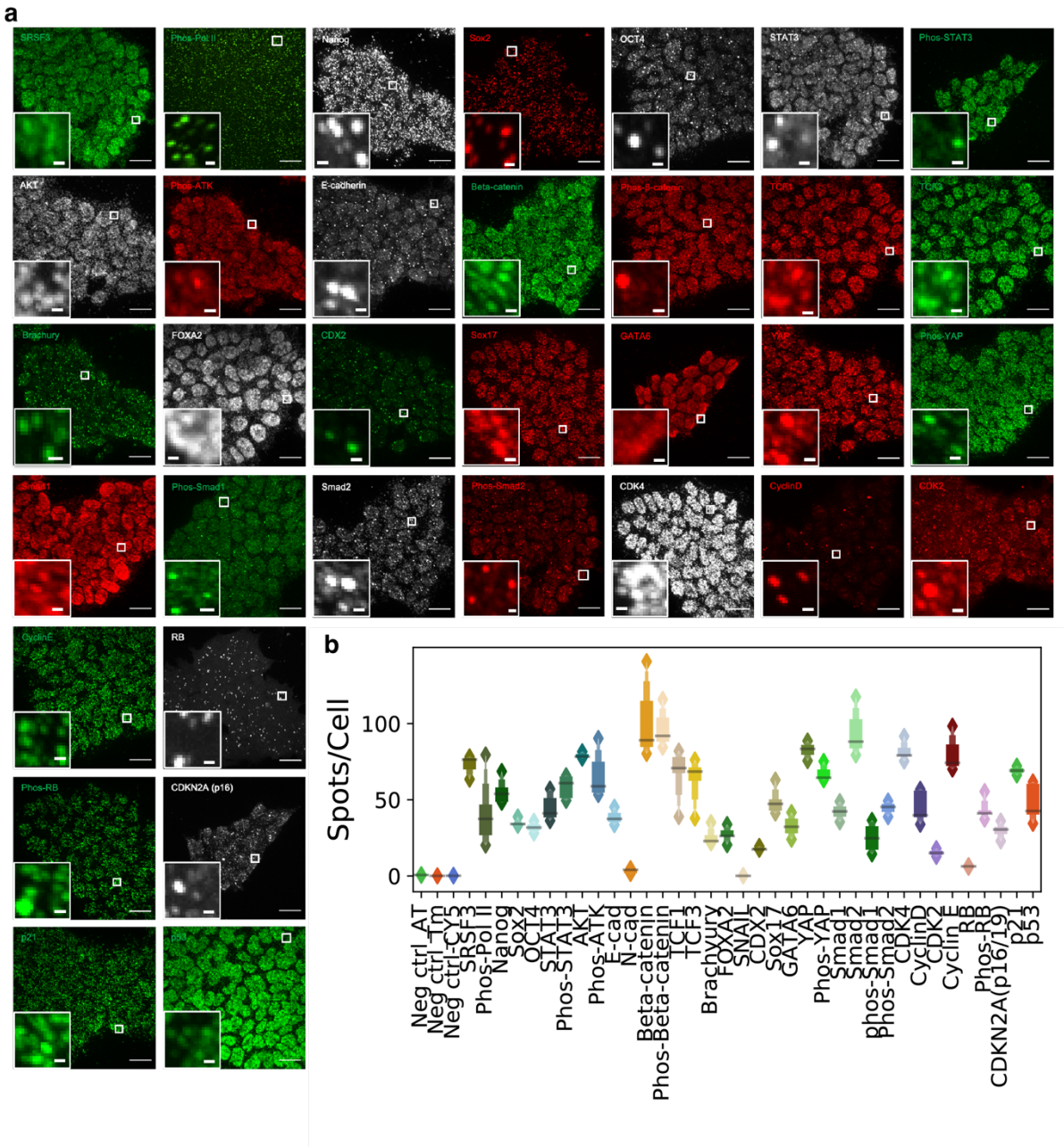

Extended Data Fig. 3: Validation of protein targets by ARTseq-FISH.
a, Representative max intensity and Z projection images of each protein target. Zoomed images show representative spots. Scale bar, 20 µm and 1 µm. **b,** Quantification of spots per cell for validated antibodies. Negative controls were incubated without antibodies. (Neg ctrl n=303, SOX2 and RB n=365, Phos-AKT, Brachyury and Nanog n=477, SRSF3, Phos-Smad2, and STAT3 n=265, Cyclin E, Phos-Beta-catenin and OCT4 n=223, CDKN2A, GATA6 and Phos-STAT3 n=222, Beta-catenin and Smad2 n=226, Phos-YAP and Smad1 n=319, P21, CDK2 and E-cadherin n=232, CDX2, YAP and AKT n=212, TCF3, TCF7 and FOXA2 n=314; Phos-RB, SOX17 and CDK4 n=366, Cyclin D and p53 n=395, phos-Smad1 n=652, Phos-Pol II n=1000, Snail1 n=263).

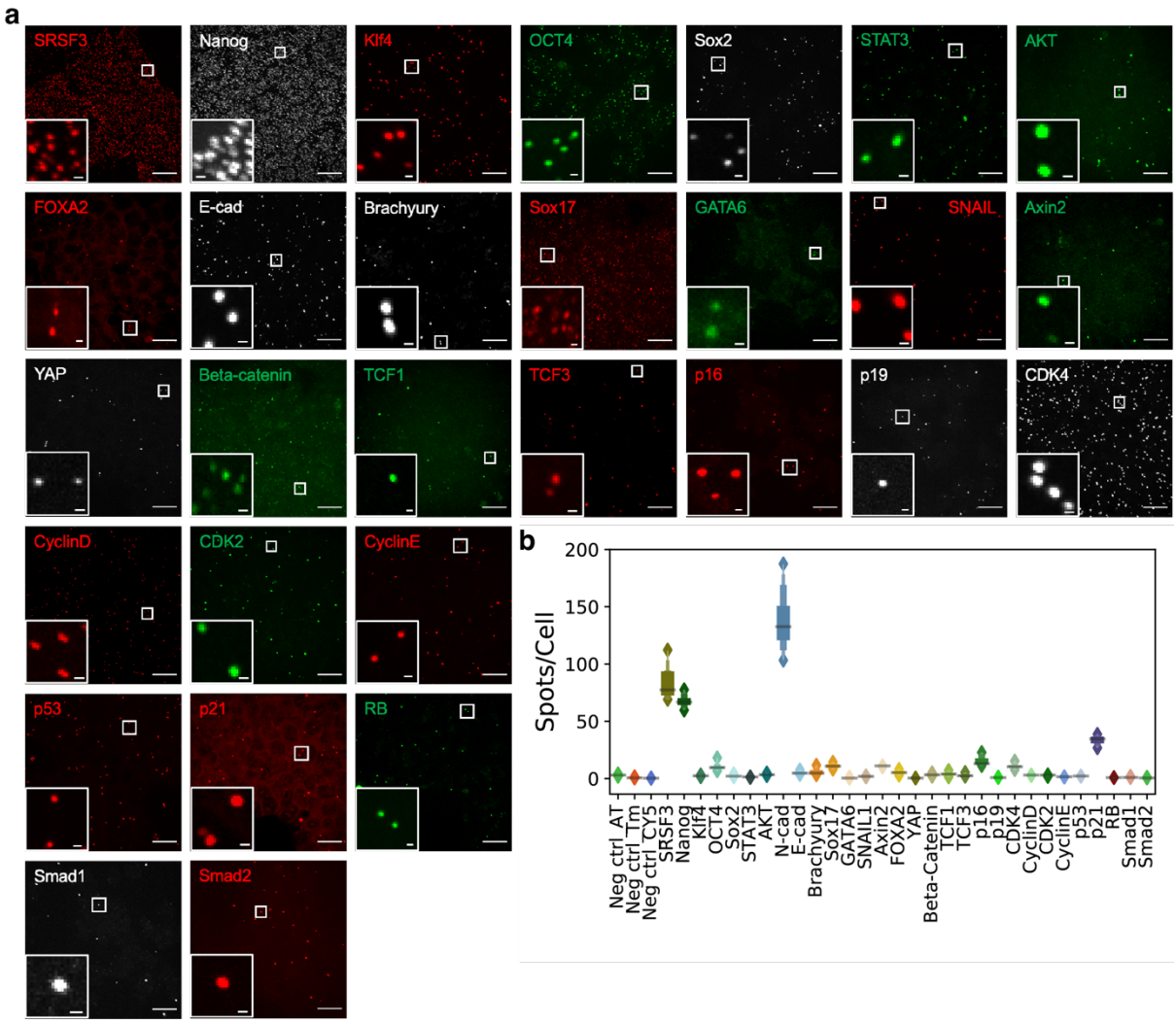

Extended Data Fig. 4: Validation of mRNA targets by ARTseq-FISH.
a, Representative max intensity and Z projection images of each mRNA target. Zoomed images show representative spots. Scale bar, 20 µm and 1 µm. **b,** Quantification of spots per cell for targeted mRNAs. Negative controls were performed without PLPs. (Neg ctrl n=579, AKT and Smad2 n=455, TCF1, TCF3 and Brachyury n=503, FOXA2, E-cadherin n=470, CDK2, CDK4 and SNAIL n=482, Axin2 and CyclinD n=454, GATA6, p16 and Smad1 n=466, Klf4 and p19 n=488, Oct4, Nanog and Sox2 n=408, p53 n=180, Sox17 and Beta-catenin n=241, STAT3 and CyclinE n=200, YAP, RB and p21 n=233).

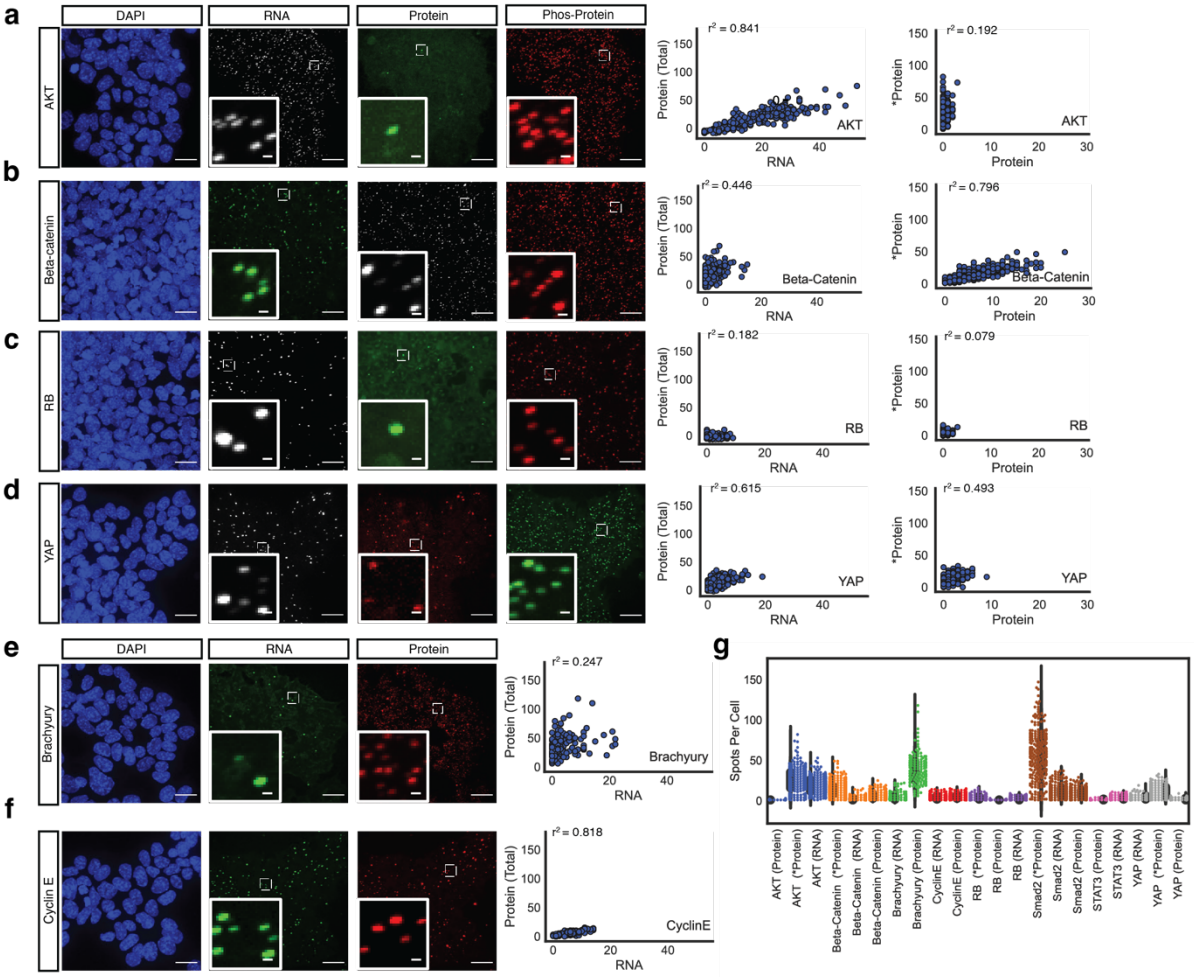

Extended Data Fig. 5: Simultaneously detection of mRNA (protein) and corresponding protein (phosphoprotein) by ARTseq-FISH in single cells.

a-f, Representative max intensity and z-projection images showing simultaneous detection of mRNAs and their proteins, phosphorylated proteins by ARTseq-FISH. Zoomed images show the comparable size of mRNAs and proteins spots acquired by ARTseq-FISH. Scale bar, 20µm, 1µm. Single-cell correlation plot of selected mRNAs targets with their proteins, proteins with their phosphorylated proteins. **g** Quantification of the abundance of the selected targets at a single-cell level. *Protein represents phosphorylated proteins. (AKT n=539; Beta-catenin n=452, Brachyury n=367, CyclinE n=389, RB n=637, Smad2 n=529, STAT3 n=498; YAP n=437;).

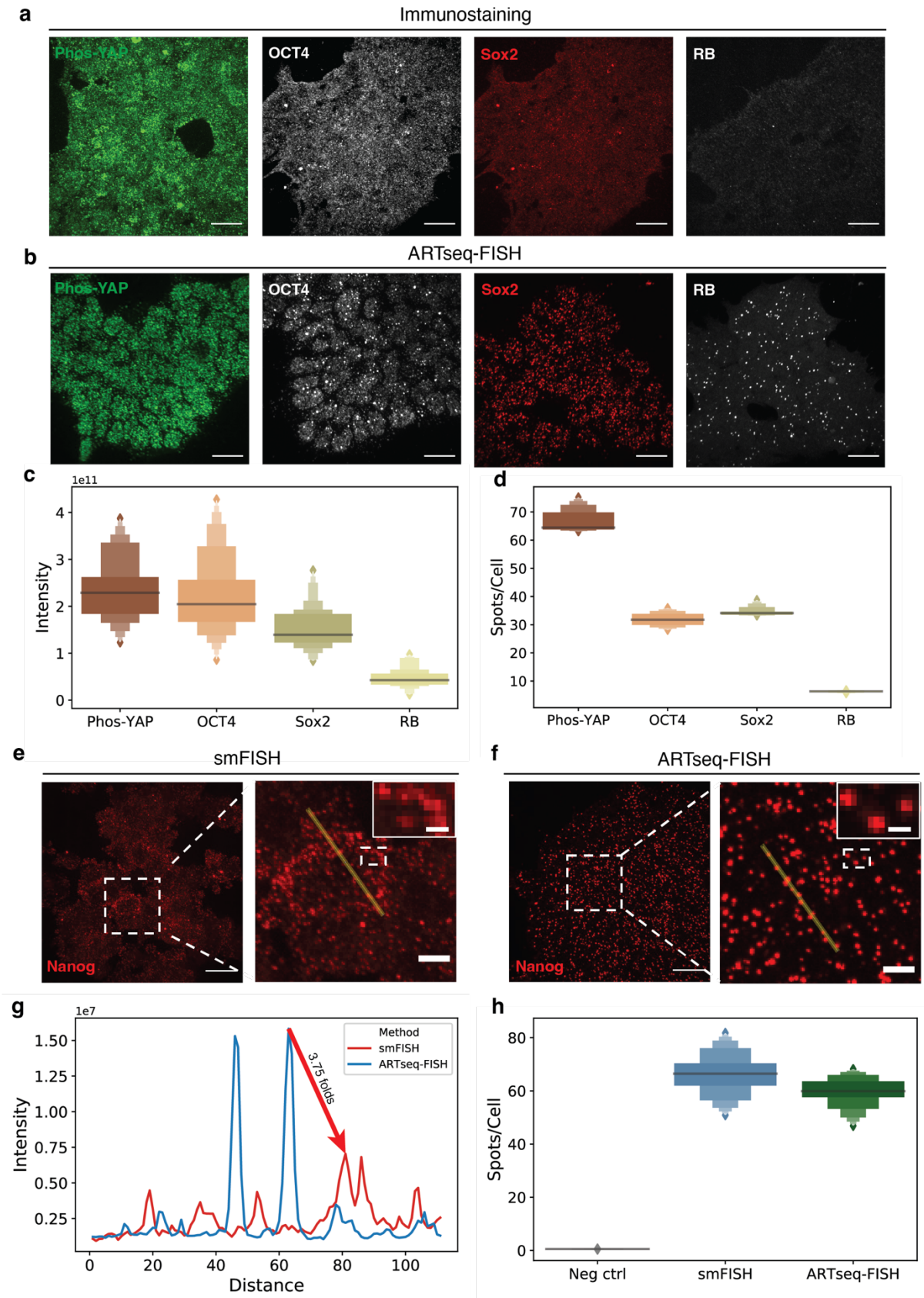

Extended Data Fig. 6: Comparison between ARTseq-FISH with conventional methods. **a and b,** Rrepresentative max intensity and Z projection images of selected antibodies detected by immunostaining and Ab-FISH. Scale bar, 20 µm. **c,** Measuring cell fluorescence in immunostaining images of selected antibodies (Phos-YAP, OCT4, Sox2 and RB) with

corrected total cell fluorescence (CTCF). CTCF = Total cell intensity - (area of selected cell * mean background intensity). The selected cells of each antibody were from three different images. And 10 cells are selected from each image. The mean background intensity is the average fluorescence reads of 10 areas in these three images. **d,** Quantification of spots per cell of selected antibodies (Phos-YAP, OCT4, Sox2 and RB) applied in Ab-FISH. The counting results of each antibody match the trends of fluorescence intensity of each antibody shown in panel. **e-h** Nanog mRNA detected by RNA RCA-FISH and conventional smFISH. **e and f** Representative max intensity and Z projection images show mRNA spots from these two methods. Zoomed images show the representative spots. Scale bar, 20 µm, 5 µm and 1 µm. **g,** Line plot illustrated the gray value of selected spots in zoomed images in panel **e and f**. The signal to noise ratio in RNA RCA-FISH is much higher than in smFISH. Arrow shows the representative differences of the signal to noise ratio in these two methods. **h,** Quantification of spots per cell of Nanog mRNA by smFISH and RNA RCA-FISH. (Neg ctrl n=241, smFISH n=203, RNA RCA-FISH n=332)

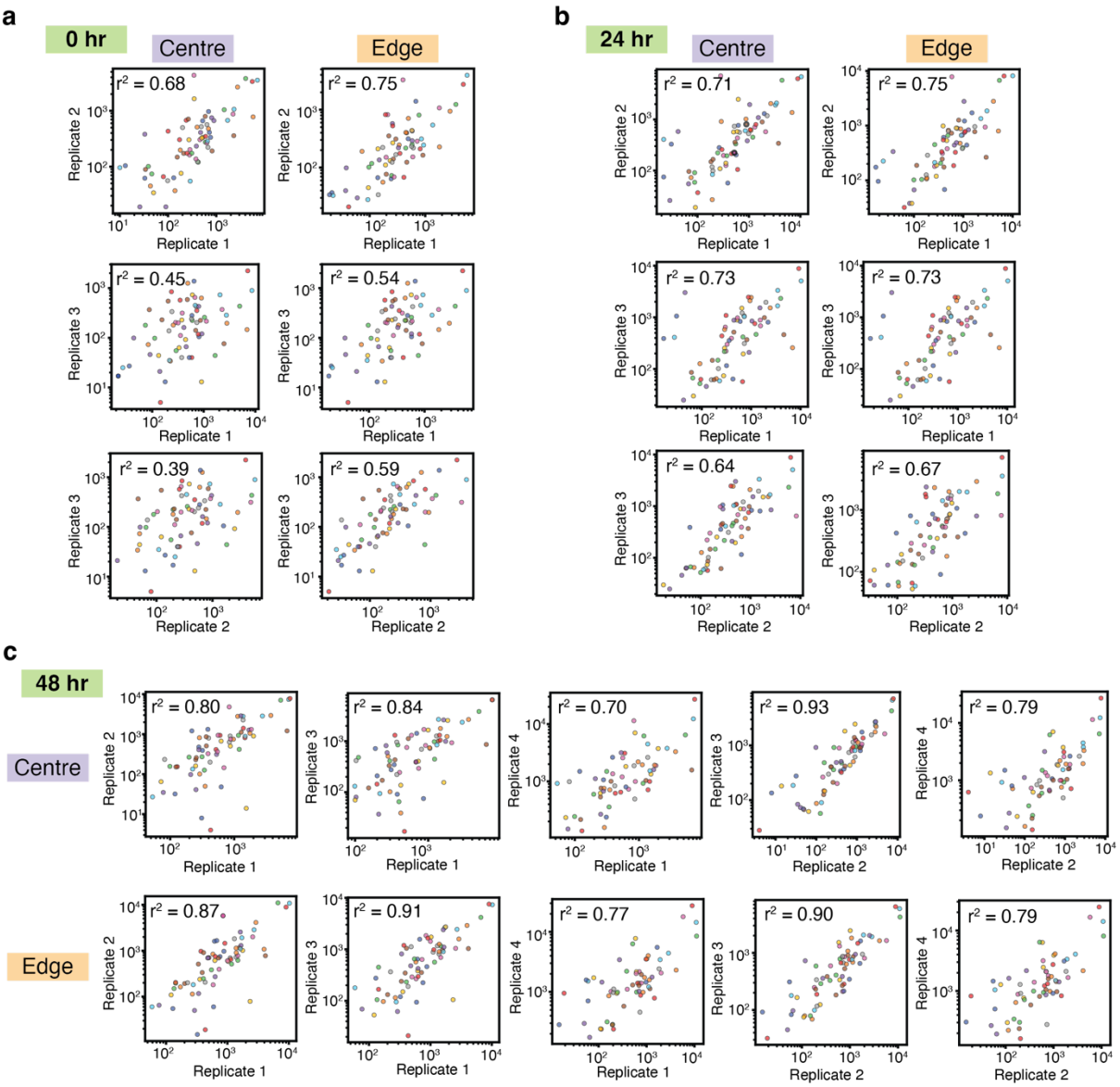

Extended Data Fig. 7: Reproducibility of ARTseq-FISH.
The correlation between different replicates of micropatterned mESCs with different positions (Center and Edge) on the micropatterns. **a,** Three replicates of micropatterned mESCs from 0 hr after LIF withdraw. **b,** Three replicates of micropatterned mESCs from 24 hr after LIF withdraw. **c,** Four replicates of micropatterned mESCs from 48 hr after LIF withdraw.

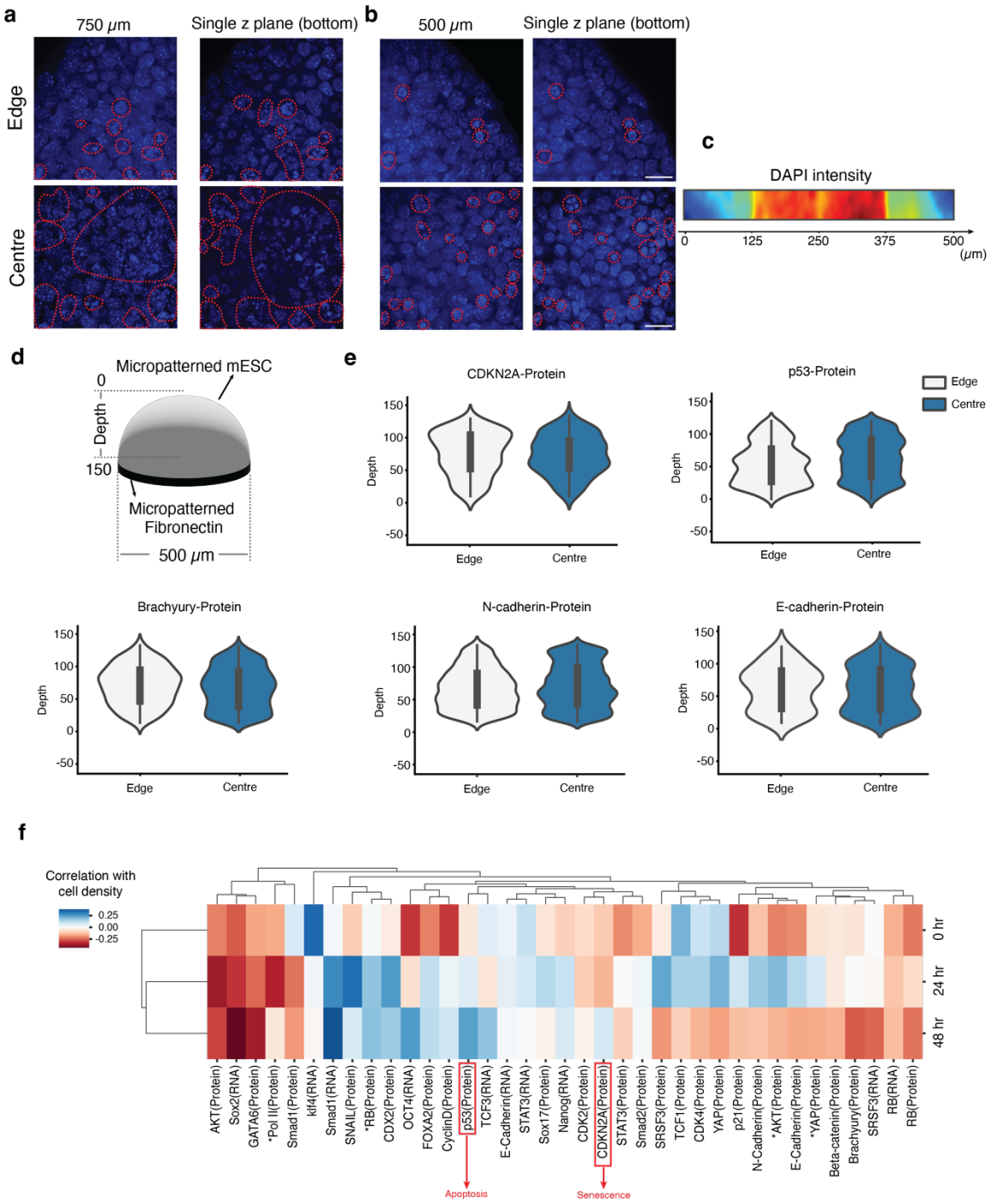

Extended Data Fig. 8: Cell density and expression profile on the micropattern.
a and b, Representative DAPI images showing the abnormal nuclei on the large micropattern (750 μm diameter) **(a)** and small micropattern (500 μm diameter) **(b)** at the edge, center and the bottom of the micropattern within the dash red line area. **c,** Normalized DAPI intensity across the micropattern (500 μm diameter). **d,** Schematic of the depth of the micropatterned mESCs on the small micropattern; **e,** Depth distribution of selected targets at the edge and center of the micropattern. The width of the violin plot represents the relative abundance. **f,** Correlation between target and cell density over time.

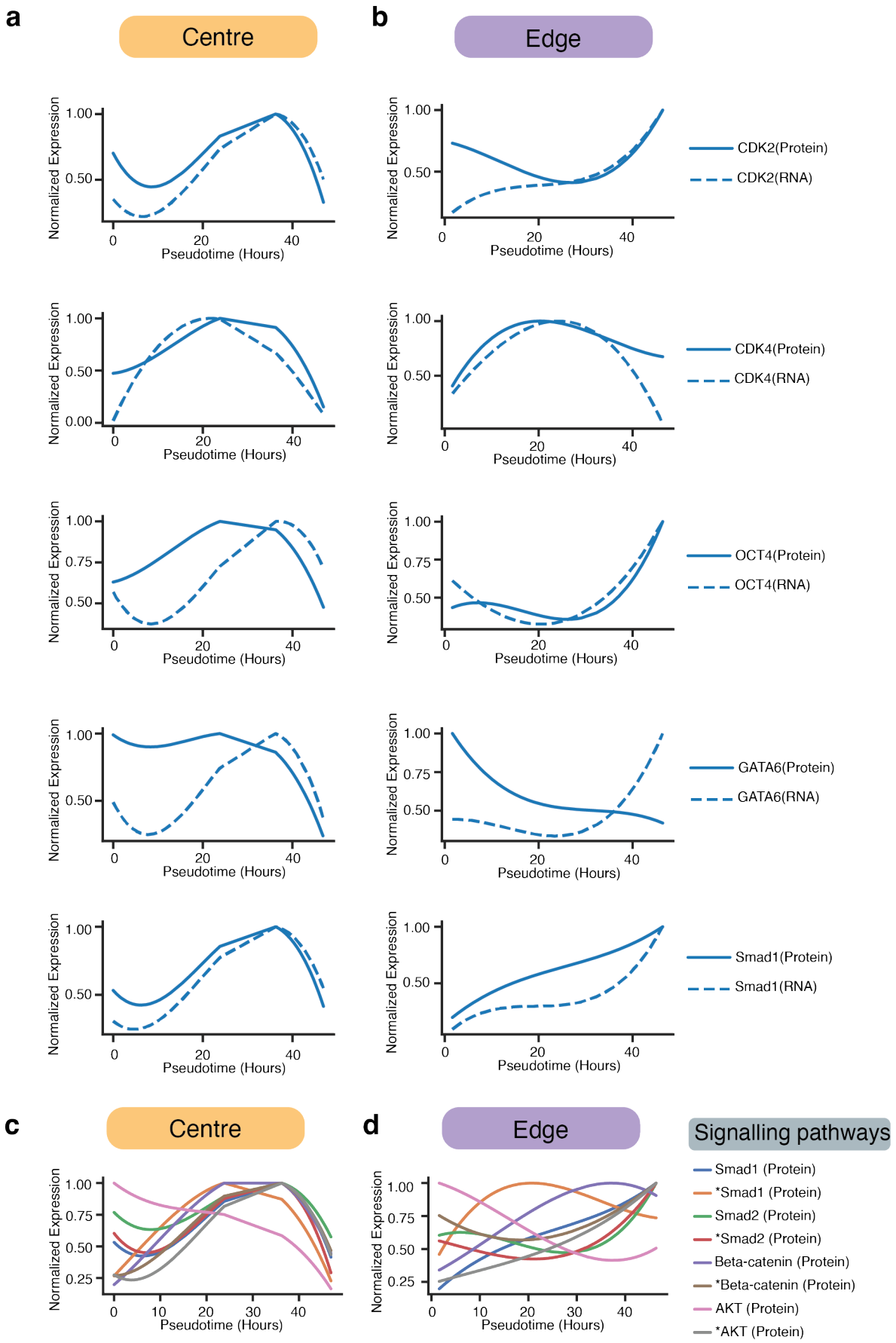

Extended Data Fig. 9: Pseudo time analysis of selected targets.

829 **a and b,** Pseudo time analysis showing the representative mRNA and its corresponding protein
830 expression trajectory at the center **(a)** and edge **(b)** of the micropattern. **c and d,** Pseudo time
831 analysis of the expression trajectory of the BMP, NODAL, WNT, and AKT signaling pathways
832 related targets at the center **(c)** and edge **(d)** of the micropattern.

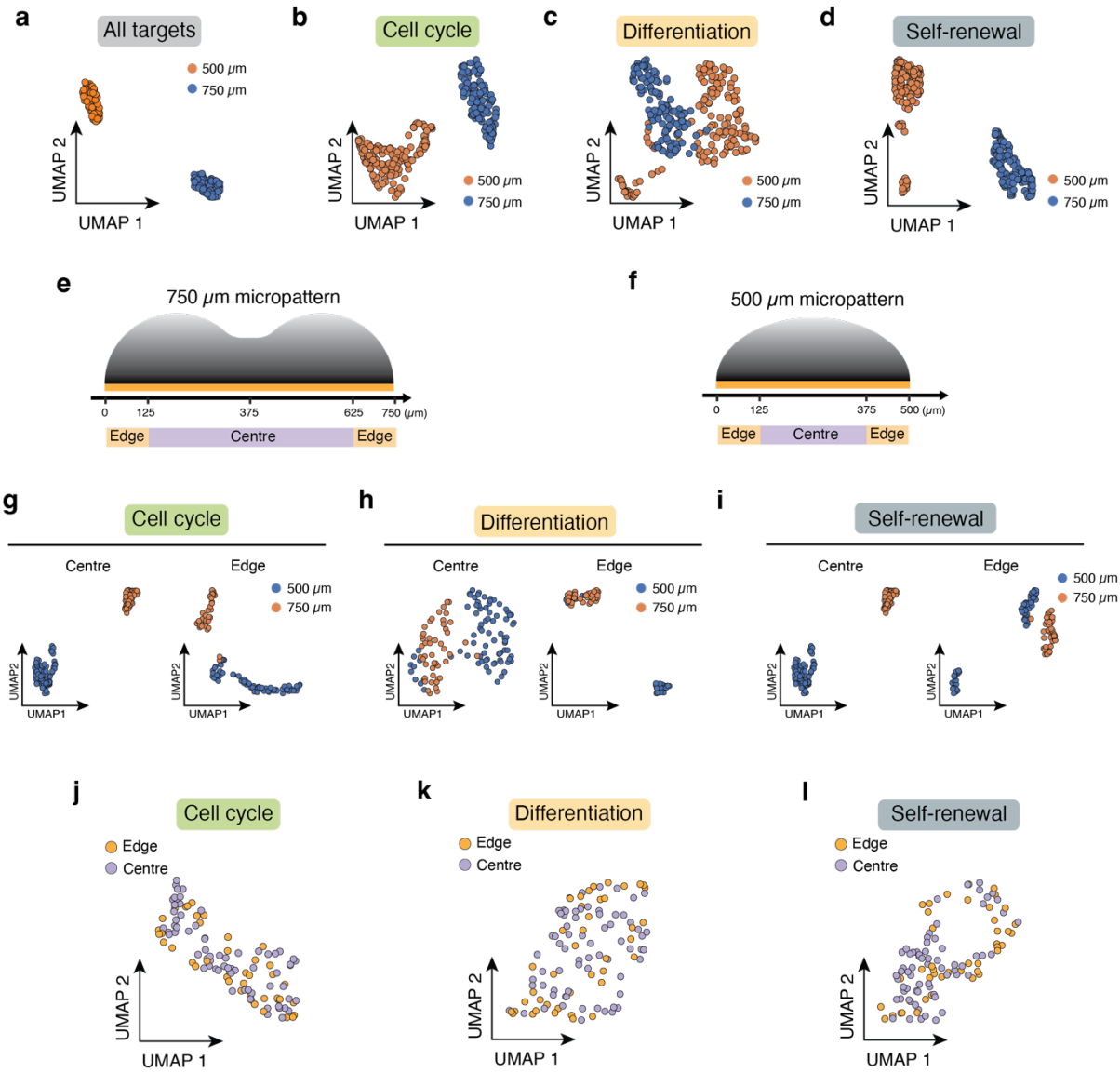

Extended Data Fig. 10: Expression profile of cell cycle, differentiation and self-renewal related targets on the small micropattern.

a, UMAP of all the detected targets from the large micropattern (750 µm diameter) and small micropattern (500 µm diameter). **b-d,** UMAP showing the expression levels of cell cycle **(b),** differentiation **(c),** and self-renewal **(d),** related targets at the large micropattern and small micropattern. **e and f,** Schematics of the defined edge and center on the large **(e)** and small **(f)** micropatterns. **g-i,** UMAP shows the expression levels of cell cycle **(g)**, differentiation **(h)**, and self-renewal **(i)** related targets at the center and edge of the large micropattern and small micropattern. **j-l,** UMAP shows the expression levels of cell cycle **(j)**, differentiation **(k)**, and self-renewal **(l)** related targets at the center and edge of the small micropattern.

Supplementary Information:

Supplementary Notes 1 Experimental development of ARTseq-FISH

Supplementary Notes 2 Computational pipeline development of ARTseq-FISH

Supplementary Figs. 1-20

Supplementary Table captions

References

Supplementary Tables 1-5